ELSEVIER

Contents lists available at ScienceDirect

Advances in Water Resources

journal homepage: www.elsevier.com/locate/advwatres





Imaging hydraulic conductivity in near-surface aquifers by complementing cross-borehole induced polarization with hydraulic experiments

Lukas Römhild a,*, Gianluca Fiandaca b, Linwei Hu c,d, Laura Meyer a, Peter Bayer a

- ^a Institute of Geosciences and Geography, Martin Luther University Halle-Wittenberg, von-Seckendorff-Platz 3, 06120, Halle (Saale), Germany
- b Department of Earth Sciences "Ardito Desio", Università degli Studi di Milano, Italy
- ^c Institute of Geosciences, Christian Albrechts University Kiel, Germany
- ^d GeoAnalysis-Engineering GmbH, Schauenburgerstraße 116, 24143, Kiel, Germany

ARTICLE INFO

Dataset link: https://doi.org/10.5281/zenodo.6 361423

Keywords: Induced polarization Hydraulic tomography Hydraulic conductivity Inversion

ABSTRACT

Precise information about the spatial distribution of hydraulic conductivity (K) in an aquifer is essential for the reliable modeling of groundwater flow and transport processes. In this study, we present results of a new inversion procedure for induced polarization (IP) data that incorporates petrophysical relations between electrical and hydraulic parameters, and therefore allows for the direct computation of K. This novel approach was successfully implemented for the Bolstern aquifer analog by performing synthetic IP experiments with a combined surface and cross-borehole setup. From these data, the distribution of K was retrieved with high accuracy and resolution, showing a similar quality compared to images achieved by hydraulic tomography. To further improve the quantitative estimates of K, we use synthetic pumping test data to inform two novel calibration strategies for the IP inversion results. Both calibrations are especially helpful for correcting a possible bias of the IP inversion, e.g., due to resolution limitations and/or to bias in the underlying petrophysical relations. The simulation of tracer experiments on the retrieved tomograms highlights the accuracy of the inversion results, as well as the significant role of the proposed calibrations.

1. Introduction

Tomographic methods have evolved as a promising family of hydrogeological field investigation techniques for imaging the hydraulic conductivity (K) distribution (Yeh and Liu, 2000; Vasco et al., 2000; Jimenez et al., 2013; Zhao and Illman, 2018; Pouladi et al., 2021). They rely on sending and recording multiple signals at different positions of an aquifer. By processing all signals together, the spatial distribution of hydraulic parameters is reconstructed. The choice of a tomographic configuration for identification of subsurface structures is rooted in geophysical exploration (Gottlieb and Dietrich, 1995; Yeh and Lee, 2007). Accordingly, tomographic concepts based on classical hydrogeological field techniques with hydraulic stimulation or tracer signals often adopt data inversion principles that are established in geophysics (Hu et al., 2011; Kong et al., 2018; Ringel et al., 2021). Vice versa, especially near surface geophysical techniques such as ground penetrating radar, electrical resistivity tomography or electromagnetic induction are tuned to not only identify geological but also hydraulic structures (Slater, 2007; Linde et al., 2006; McLachlan et al., 2021).

Still, hydraulic or tracer tomography is not fully established in practice. A major reason is the rather high experimental demand for

installation of field equipment and borehole devices (Bohling and Butler, 2010; Brauchler et al., 2013b; Cardiff et al., 2013; Klepikova et al., 2020). Fast applicability in the field is an advantage of many geophysical techniques. However, a common shortcoming is that aquifer heterogeneities are described by geophysical proxy parameters. As classical geophysical exploration techniques do not test hydraulic properties directly, their capacity to provide meaningful hydrogeological insight in aquifers is limited. Ideally, geophysical and hydrogeological information is thus jointly processed for obtaining hydrogeophysical tomograms to benefit from the advantages of both approaches (Irving and Singha, 2010; Vilhelmsen et al., 2014; Ahmed et al., 2016).

In the growing research field of hydrogeophysics (Binley et al., 2015) a strong focus is on electrical methods due to their ability of sensing pore space properties that govern the hydraulic parameters (Revil et al., 2012a; Wang et al., 2021). However, imaging hydraulic conductivity requires the separation of pore volume and pore surface properties, which cannot be achieved by conventional geoelectrical methods. As a remedy, the additional information contained in induced polarization (IP) measurements about electrical polarization effects at

E-mail address: lukas.roemhild@geo.uni-halle.de (L. Römhild).

Corresponding author.

the pore–matrix-interface can be used to quantitatively separate these properties (Slater, 2007).

To link the electrical parameters of IP measurements with the hydrogeological parameters, we mainly rely on empirical relations derived from laboratory measurements. The first quantitative relation between IP parameters and *K* was established by Börner et al. (1996). Since then, a variety of other empirical laws has been derived by spectral induced polarization (SIP) laboratory measurements (Slater and Lesmes, 2002; Binley et al., 2005; Revil and Florsch, 2010; Titov et al., 2010; Revil et al., 2012b; Attwa and Günther, 2013; Weller et al., 2015; Robinson et al., 2018).

Most of the IP parameters that are valuable for estimating K are defined in the frequency domain, as e.g., the Cole-Cole parameters (Cole and Cole, 1941; Pelton et al., 1978), and can therefore be most easily derived from SIP measurements. However, although some applications of SIP in the field do exist (Kemna et al., 2012; Orozco et al., 2012; Gallistl et al., 2018), this method is mainly used for the electrical characterization of rocks in the laboratory (Revil et al., 2014; Börner et al., 2017; Römhild et al., 2019), whereas for field campaigns time domain IP (TDIP) measurements are most common (Kemna et al., 2004; Gazoty et al., 2012; Doetsch et al., 2015). This gap can be overcome by using a Fourier transform within the IP inversion procedure, so that TDIP data can be inverted for frequency domain parameters, such as Cole-Cole parameters (Fiandaca et al., 2012, 2013) or other reparameterizations of the Cole-Cole model (Fiandaca et al., 2018a). This approach yields results of a similar quality compared to frequency domain measurements (Madsen et al., 2017), but often has an advantage in terms of acquisition time (Maurya et al., 2018b; Martin et al., 2020).

In several studies, K has already been estimated from these electrical parameters at field scale (Hördt et al., 2009; Attwa and Günther, 2013; Maurya et al., 2018a). However, the petrophysical relations mentioned above have always been applied after the inversion for IP parameters, making the interpretation in terms of hydraulic parameters ambiguous. Instead, incorporating the petrophysical laws into the inversion procedure allows the direct computation of the K-distribution in the subsurface from the measured IP data. Although ambiguities might also be reduced with strong structural priors such as training images (Pirot et al., 2017), a petrophysical inversion approach can have further advantages. By introducing a new parameterization, parameter correlations can be reduced, and the direct inversion for K makes it easier to study its uncertainties and how data errors propagate to model errors. It also allows to apply the regularization to the actual hydraulic parameters instead of the electrical parameters and simplifies the integration of prior models that are often given as a distribution of K. Petrophysical inversion strategies have already been applied in other contexts, such as permafrost sites (Mollaret et al., 2020), gas hydrate systems (Turco et al., 2021) or reservoir characterization (Gao et al., 2012), but mostly with the aim of establishing a joint inversion.

While our new IP-K inversion approach has already been mentioned briefly in conference abstracts (Fiandaca et al., 2021; Martin et al., 2021), we now present the complete methodology and a detailed assessment of the results for the first time. We are aiming to show the abilities and limitations of this deterministic inversion for imaging K-heterogeneities in near-surface aquifers by performing synthetic modeling and inversion tests on aquifer analog data with a combined surface and cross-borehole IP setup. We compare those results with data derived from synthetic hydraulic tomography (HT) experiments using a similar setup. Our main goal is to achieve a distribution of K that would yield a correct solute transport simulation. For this purpose, a straightforward calibration strategy of complementing IP inversion with hydraulic information is introduced.

In the following, we briefly explain the methodological concepts of IP and HT, as well as our new IP-K inversion approach. As the study site for simulating a synthetic cross-hole HT and IP application, a sedimentary aquifer analog is implemented to compare the abilities of the two methods in imaging decimeter-meter scale K-heterogeneities with varying point spacing. The performance of the new calibration strategy is evaluated and all findings are discussed with special emphasis on the applicability of the suggested methodology within field campaigns.

2. Materials and methods

Fig. 1 gives an overview of the procedures applied in this study. The Bolstern aquifer analog (Heinz et al., 2003) serves as the input data set for the forward modeling of IP data and the HT synthetic experiments. The achieved data sets are then used for the respective inversion (the new IP-K inversion procedure and an HT travel time inversion). Additionally, we achieve an effective hydraulic conductivity K_{eff} as an average value for the whole domain by a small set of seven pumping tests and use it to calibrate our inversion results. To assess the quality of those calibrations and the performance of the two methods in general, we finally conduct tracer transport simulations with the achieved K tomograms and evaluate them based on imaged tracer plumes as well as depth-integrated tracer breakthrough curves.

2.1. Bolstern aquifer analog

The Bolstern aquifer analog data set (Heinz et al., 2003) was derived from an outcrop analog study of fluvial deposits located near Bolstern (SW-Germany, see Fig. 2a) within the paleo-discharge zone of the Rhine glacier. The analog study comprises a rectangular $20 \text{ m} \times 7 \text{ m} 2D$ cross-section (Fig. 2b), which is built up by a mosaic of hydrofacies units that were delineated from the outcrop wall at a resolution of 0.05 m. The hydrofacies units represent nearly hydraulically homogeneous units with K derived from grain size analysis, as well as porosity information. The hydrofacies accord with the sedimentary lithofacies, and this is reflected in the structural features of the analog, with heterogeneous layers and cross beddings as a common characteristic for many sedimentary unconsolidated aquifers. The Bolstern analog has already been used as a realistic test case for modeling contaminant transport in previous work (Höyng et al., 2015).

We use a section of the whole analog between x = 0 m and 12 m (which corresponds to x = 6 m and 18 m in the original nomenclatures of Heinz et al. (2003)), covering the whole depth range from z = 0 m to -7 m (red rectangle in Fig. 2b). For all simulated virtual experiments we assume to have three boreholes at x = 3 m, 6 m and 9 m (black lines in Fig. 2b).

2.2. Induced polarization

2.2.1. Electrical rock properties

The electrical conductivity σ^* of a rock is generally considered to be a frequency-dependent and complex-valued quantity (Olhoeft, 1985)

$$\sigma^*(\omega) = \sigma_{el} + \sigma_{int}^*(\omega) \tag{1}$$

consisting of electrolytic conductivity σ_{el} and interface conductivity σ_{int}^* , with $\omega=2\pi f$ being the angular frequency and the * denoting complex quantities. It can be written in terms of real and imaginary part (σ' and σ'' , respectively) or as magnitude $|\sigma^*|$ and phase angle φ

$$\sigma^*(\omega) = \sigma'(\omega) + i\sigma''(\omega) = |\sigma^*| \cdot e^{i\varphi},\tag{2}$$

where i is the imaginary unit. The electrolytic part is controlled by the conduction through a rock's pore space and thus depends on pore volume properties as described by Archie's Law (Archie, 1942)

$$\sigma_{el} = \frac{\sigma_w}{F} = \phi^m \cdot \sigma_w, \tag{3}$$

where σ_w is the pore water conductivity, $F = \phi^{-m}$ is the formation factor, ϕ is porosity and m is the empirical cementation exponent. This formulation assumes fully saturated conditions.

The interface conductivity σ_{int}^* , however, may contain contributions from a variety of electrical polarization phenomena that are mainly related to the interface between rock matrix and pore space. If electronically conductive minerals, such as graphite or pyrite, are absent, as it is mostly the case in sedimentary environments, diffusion-related

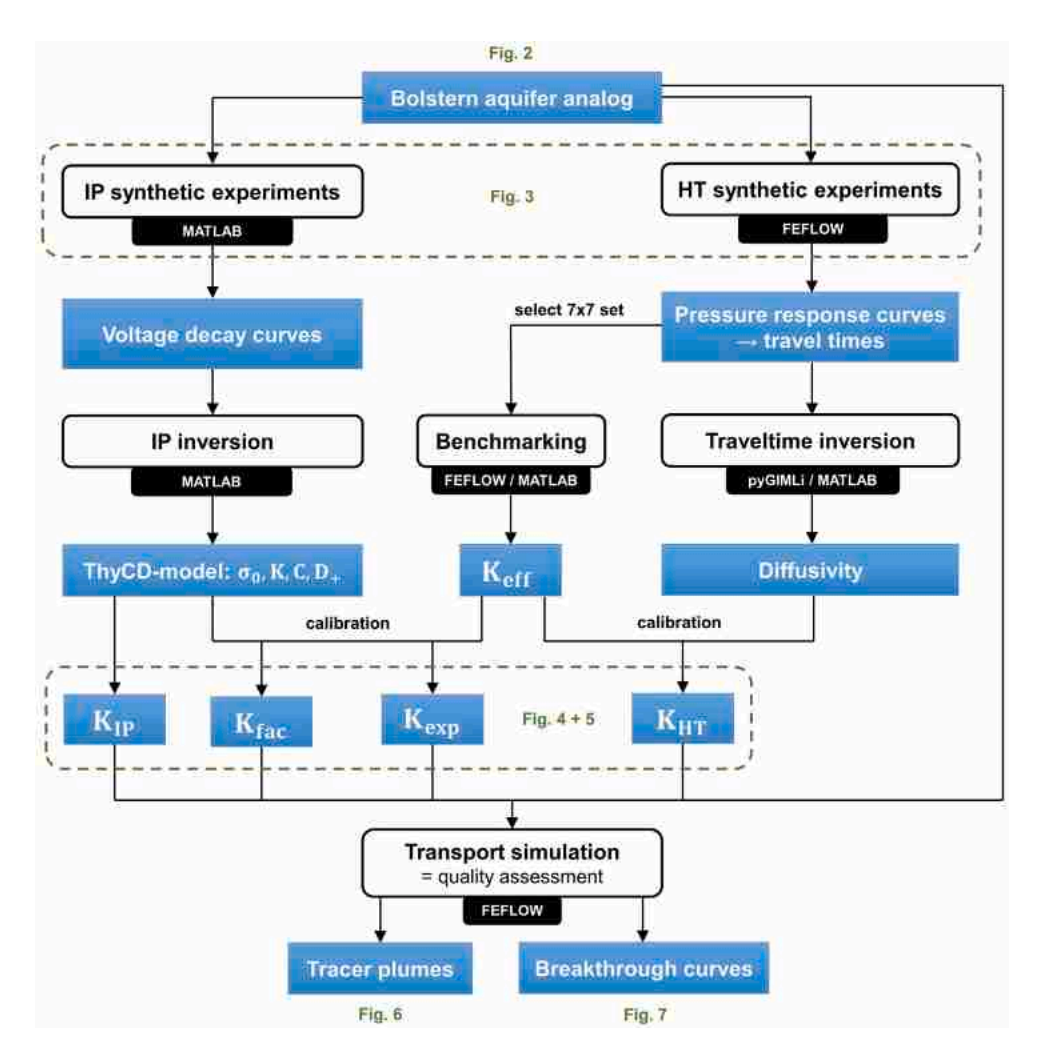


Fig. 1. Workflow for imaging K in heterogeneous aquifers with induced polarization (IP, left section) and hydraulic tomography (HT, right section). Blue boxes represent any type of data and black boxes contain the different processing steps. The green labels refer to the other figures in this work.

polarization connected to the electrical double layer (EDL) at the pore-matrix-interface is dominant (Marshall and Madden, 1959; Schwarz, 1962).

While standard geoelectrical methods are only sensitive to the real part σ' of the electrical conductivity, IP measurements can retrieve information about the imaginary part σ'' as well. This is either done by conducting spectral induced polarization (SIP) measurements in the frequency domain and then converting the magnitude and phase angle information to a complex electrical conductivity, or by performing time domain induced polarization (TDIP) measurements and full-decay spectral inversion (Fiandaca et al., 2012, 2013; Madsen et al., 2020). We will focus on the latter option since the acquisition time is smaller in the field (Maurya et al., 2018b) and a good retrieval of spectral properties is achievable when a wide time range is used in acquisition (Madsen et al., 2017), for instance through the analysis of full-waveform recordings (Olsson et al., 2016).

A typical TDIP field setup is similar to a standard DC geoelectrics setup with a sequence of quadrupoles injecting a current with two electrodes (A, B) and measuring the resulting voltage with two other electrodes (M, N). A simplified setup is shown in Fig. 3a. The sequence is typically distributed along a 2D profile on the surface, e.g., following a gradient protocol (i), and can be complemented by cross-borehole measurements (ii) or quadrupoles in a single borehole (iii). For the

synthetic experiments carried out within this study, a combination of the three options shown in Fig. 3a is used, but a variety of other sequences is possible (Bing and Greenhalgh, 2000). While surface IP measurements are becoming a more widely used method, field examples of cross-borehole IP are still rare (Kemna et al., 2004; Binley et al., 2016; Bording et al., 2019).

To extract meaningful parameters from IP data, the Cole–Cole model is commonly used to describe the spectral behavior of σ^* (Cole and Cole, 1941; Pelton et al., 1978; Tarasov and Titov, 2013):

$$\sigma^*(\omega) = \sigma_0 \left[1 + \frac{m_0}{1 - m_0} \left(1 - \frac{1}{1 + (i\omega \tau_{\sigma})^c} \right) \right]. \tag{4}$$

Here, σ_0 is the DC conductivity, m_0 the intrinsic chargeability as defined by Seigel (1959), τ_σ the relaxation time and c the frequency exponent.

Based on petrophysical relations found in laboratory studies, the electrical properties of a rock can be used to predict hydraulic conductivity K. In the following, we make use of two different approaches. First, Revil et al. (2012b) found a relation for permeability k (and hence hydraulic conductivity K) based on relaxation time τ_{σ} , formation factor F and the diffusion coefficient of the Stern layer D_+ :

$$k = \frac{\tau_{\sigma} D_{+}}{4E}.$$
 (5)

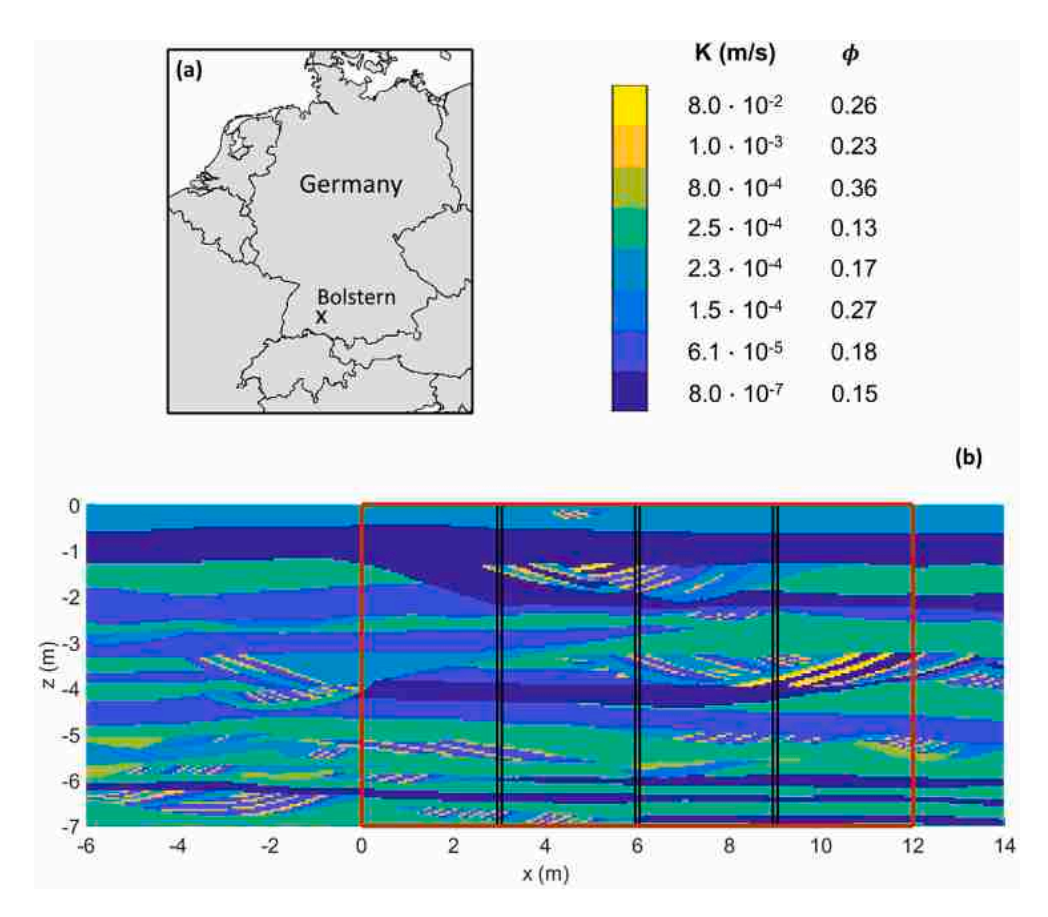


Fig. 2. (a) Location of the Bolstern aquifer analog in SW-Germany and (b) visualization of the data set as a 2D cross-section including the heterogeneities of hydraulic conductivity K and porosity ϕ . The red rectangle indicates the section of the data set used in this work and the black lines represent the three hypothetical boreholes at x = 3 m, 6 m and 9 m.

A powerlaw fit of $R^2=0.88$ was reported for the used set of clean saturated sand samples. The relation is based on the idea that τ_σ can be treated as a measure for typical scale lengths (e.g., pore throat size), that in return govern the hydraulic conductivity. The volumetric properties are accounted for by F as a measure for effective porosity. At first sight, this approach does not include any empirical parameters and should be straight-forward to use. However, while τ_σ and F can be directly derived from the IP measurements, the diffusion coefficient D_+ can only be estimated, typically depending on the clay content. Revil et al. (2015) give the following values for clean sand and clay:

$$D_{+,sand} = 1.3 \cdot 10^{-9} \cdot \text{m s}^{-2}, \tag{6}$$

$$D_{+,clay} = 3.8 \cdot 10^{-12} \cdot \text{m s}^{-2}.$$
 (7)

However, other laboratory findings are raising doubt about the existence of two distinct values for D_+ (Weller et al., 2016). Instead, an apparent diffusion coefficient D_a can be introduced that may cover a much wider range of values, although its physical significance remains unclear. In our study, in which sand–clay mixtures are actually reflected in a wide range of K-values, we still use the two values given by Revil et al. (2015) to compute a distribution of D_+ directly from K by imposing an interpolation in logarithmic space. However, the purpose of this simplification is only the simulation of realistic τ_σ -values (according to Eq. (5)) within the forward modeling.

The second petrophysical approach was introduced by Weller et al. (2015). It uses the formation factor F and the imaginary part σ''

evaluated at a frequency of 1 Hz for permeability estimation:

$$k = \frac{\alpha}{F^{\beta} \left(\sigma''(1 \text{ Hz})\right)^{\gamma}} \tag{8}$$

with the empirical parameters $\alpha=1.08\cdot 10^{-13},\ \beta=1.12$ and $\gamma=2.27$ for unconsolidated and fully saturated sediments. The coefficient of determination is reported as $R^2=0.862$ and an additional degree of uncertainty lays in the applicability of the empirical parameters $\alpha,\ \beta$ and γ in the given geological setting.

Furthermore, we use a relationship between imaginary and real part of surface conductivity found by Weller et al. (2013):

$$\sigma''(1 \text{ Hz}) = l \cdot \sigma'_{int}(1 \text{ Hz}) \tag{9}$$

with $l = 0.042 \pm 0.022$, but imposing the relation at the frequency $f = (2\pi\tau_{\sigma})^{-1}$ (Fiandaca et al., 2018b).

Finally, the conversion from permeability k to hydraulic conductivity K can be achieved by

$$K = \frac{d \cdot g}{\eta} \cdot k,\tag{10}$$

where d is the density of the pore fluid, g the gravitational acceleration and η the dynamic viscosity of the pore fluid. Assuming a groundwater temperature of 10 °C we use the approximation

$$K = 7.5 \cdot 10^6 \cdot k. \tag{11}$$

For more details on the petrophysical background we refer to Fiandaca et al. (2018b) and the references therein.

Clearly, all petrophysical laws between hydraulic and electrical parameters are only approximations that bear a significant amount of

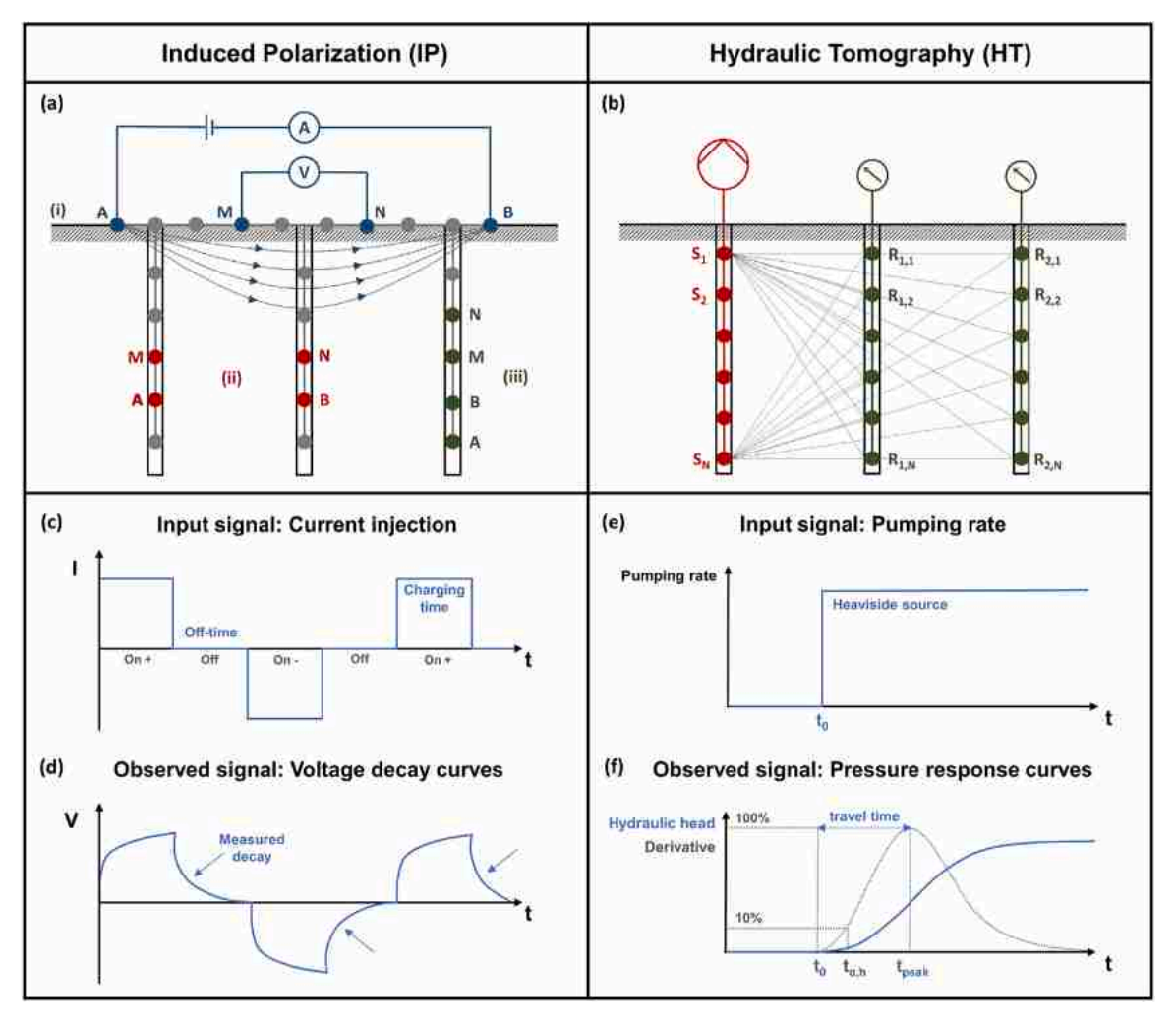


Fig. 3. Comparison of induced polarization (left section) and hydraulic tomography (right section) experimental setups as well as simplified input and output signals. (a) Typical IP setup with current electrodes A, B and voltage electrodes M, N distributed (i) on a surface profile, (ii) as a cross-borehole setup or (iii) in a single borehole. (b) Typical HT setup with source points S_1 ... S_N (pumping locations) in the left borehole and receiver points S_1 ... S_N (observation locations) in the two other boreholes. (c) Input signal of the injected current: rectangular function with alternating polarity. (d) Observed voltage signal: decay curves reacting to the injected current and the polarization effects in the rock's pore space. (e) Pumping signal in the source points following a Heaviside function. (f) Observed pressure response curves at the receiver points with peak time t_{peak} and early time $t_{a,h}$ according to the 10%-diagnostics approach.

uncertainty. Additionally, due to the regularization applied within the inversion, the petrophysical relationships of the tomograms are also resolution-dependent (Hermans and Irving, 2017). Although we will show how these regularization-induced errors as well as a simple bias in the petrophysical relations can partly be corrected by our proposed calibrations, their intrinsic scatter can barely be reduced by these procedures. Especially in strongly heterogeneous aquifers (like the Bolstern aquifer) this uncertainty can be significant, easily spanning one to two orders of magnitude (e.g., Hördt et al. (2009)). In addition, further parameters (like the cementation exponent m) that are approximated as constants, might be spatially variable (Schön, 2015; Yue, 2019). Therefore, petrophysical relations actually present in the field are often far from the laws derived in the lab (e.g., Benoit et al. (2019)), so that not only the inherent uncertainty, but also the applicability of those relations in a given field setting are limiting factors for the quality of the inversion result. Synthetic experiments should always be regarded as best case scenarios showing the upper limit of K-prediction quality that may be achieved in a field application. However, even best-case scenarios are anything but trivial, and insights from synthetic studies

are important means to judge the role of procedural assumptions for an inversion and the resolution capability of the proposed methods.

2.2.2. Forward modeling

For defining the input data set used within the forward simulation, the WhyCDF model space

$$\mathbf{m}_{WhyCDF} = \{\sigma_w, K, D_+, F, c\} \tag{12}$$

was used. The WhyCDF acronym indicates the model parameters, i.e. water and hydraulic conductivity σ_w and K, respectively, diffusion coefficient D_+ and formation factor F (the frequency exponent c is not specified in the acronym). The idea of re-parameterizing the model space is based on Fiandaca et al. (2018a), now being extended by directly imposing the petrophysical relations (Eqs. (1), (2), (4), (5), (8), (9) and (11)) onto the objective function. Therefore, the conversion from hydrological to electrical parameters is part of the modeling process and not a separate procedure. The two petrophysical approaches by Revil et al. (2012b) and Weller et al. (2015) are simultaneously used by forcing them to yield the same permeability k. The five different input parameters were set up in the following way:

- Water conductivity σ_w was assumed to be constant at 100 mS/m, which is a realistic value for groundwater (Schön, 2015).
- Hydraulic conductivity *K* was directly imported from the Bolstern data set (Heinz et al., 2003).
- The diffusion coefficient D_+ was derived from K by interpolation in log-space from the sand–clay values suggested by Revil et al. (2015), thereby imposing realistic τ_{σ} -values on the data.
- The formation factor F was computed from the porosity information contained in the Bolstern data set by assuming a constant cementation exponent of m = 1.3 as a realistic value for unconsolidated sediments (Schön, 2015).
- ullet The frequency exponent of the Cole–Cole model c was assumed to be constant at 0.5.

The full data set (hydraulic conductivity K, diffusion coefficient D_+ and bulk conductivity σ_0 including both F, σ_w and σ'_{int}) is shown in Appendix B.

The synthetic IP experiments are based on a setup consisting of one surface profile over the entire length of the data set ($x=0\dots 12$ m) as well as electrodes in three hypothetical boreholes at x=3 m, 6 m and 9 m. We consider this to be a realistic setup within a field study that should allow resolving the heterogeneities of the aquifer within the whole domain. Furthermore, the same setup of boreholes is expected to work well for HT, so that the results of the two methods can be compared directly. In practice, the same boreholes could be used to conduct all the experiments.

To simulate realistic field conditions, Gaussian noise of 2% and 10% magnitude was added after the forward simulation to resistivity and IP data, respectively. Field data can mostly be fitted with this level of error, as for instance demonstrated in Maurya et al. (2018a). Some exemplary decay curves with added noise and error bars of the assumed standard deviation model are depicted in Appendix B.

We run the forward simulation in 2D following Fiandaca et al. (2013) with three different electrode spacings - 1 m, 0.5 m and 0.25 m - to assess the impact of varying spacings on the inversion (in terms of computational performance and ability to image K-heterogeneities). The sequence follows a commonly used gradient protocol for the surface profile and borehole quadrupoles according to the cases (i), (ii) and (iii) shown in Fig. 3a, with IP time gates ranging from 0.003 s to 12 s. The total number of quadrupoles (from which the total duration of a field experiment might be estimated) are 162 for 1 m spacing, 885 for 0.5 m spacing and 2866 for 0.25 m spacing.

2.2.3. Inversion

The inversion was performed in the ThyCD model space

$$\mathbf{m}_{ThvCD} = \{\sigma_0, K, D_+, c\}$$
 (13)

consisting of total (DC) conductivity σ_0 , hydraulic conductivity K, diffusion coefficient D_+ and frequency exponent c. All four parameters are space-dependent and uncoupled during the inversion, but the spatial variability of each parameter can be adjusted by setting horizontal and vertical constraints.

While a model space with five parameters (like WhyCDF) is convenient as input for a forward simulation, it is not possible to invert for both the formation factor and the water conductivity, since the effects of both parameters on DC conductivity cannot be separated. Consequently, the water conductivity is considered a prior information in the inversion, and the total DC conductivity is used for the parameterization of the inversion result. This choice is supported by the results of Markov chain Monte Carlo modeling performed with different parameterizations (Fiandaca et al., 2021), where the ThyCD model space turned out to be the most suitable and is therefore used for this work. Again, it should be stressed that the conversion from electrical to hydrological parameters is an inherent part of the inversion and not a separate procedure.

Although we refer to the diffusion coefficient as D_+ here, it might also be interpreted as an apparent diffusion coefficient D_a (Weller et al., 2016) in the inversion results. We also performed additional inversion tests with a different model space, where D_+ is replaced by τ_σ , so that Eq. (5) (Revil et al., 2012b) is actually not used. The distribution of K remains almost identical, which shows that Eq. (8) (Weller et al., 2015) alone can also be sufficient for the inversion of TDIP data.

The data space of the inversion consists of the DC data and the full decays of the quadrupole sequence. The objective function, which contains the squared data misfit and smoothness regularization terms for vertical and horizontal constraints, is minimized through a iterative Gauss–Newton approach (Fiandaca et al., 2013).

We ran all the codes on a standard desktop PC with an 8-core i7-9700K 3.6 GHz processor and 32 GB RAM. The runtime for one iteration is about one minute for the 1 m spacing electrode sequence, 7–8 min for the 0.5 m sequence and around 30 min for the 0.25 m sequence, which adds up to a total inversion runtime of several hours (depending on the number of iterations) in the last case. This shows that also the inversion of field data can mostly be conducted on standard PC equipment.

2.2.4. Calibration with hydraulic data

Identification and resolution of K-heterogeneity is in particular relevant for performing transport modeling. Therefore, it is especially crucial to obtain accurate K-estimates in the preferential flow paths and thus in areas of high K. However, the strongest IP signal (e.g., in terms of chargeability) is typically measured in materials with low K since they have a higher inner surface area and therefore a more pronounced polarization connected to the EDL. In contrast, in the high-K-zones the IP signal is relatively weak, so that the K-estimates in the preferential flow paths are less supported by the IP data and might be less accurate. Considering these unfavorable properties of IP, resulting tomograms may resolve structural features very well but they are not very reliable with respect to the hydraulic characterization of preferential flow paths. Additionally, the uncertainties of the petrophysical relations linking electrical and hydraulic properties, as well as regularization effects might produce a bias in K-prediction. As a remedy, we suggest calibrating the IP inversion result by incorporating information gathered from pumping test data.

In the synthetic example, we retrieve the effective hydraulic conductivity K_{eff} as a single value for the whole domain by performing synthetic pumping tests on the Bolstern data set using Feflow. The procedure is inspired by the approach of Wu et al. (2005). A setup of seven pumping locations in the left borehole and seven observation points in the right borehole is used (see Appendix A, part c). The pumping tests are carried out in exactly the same way as the HT experiments (see Section 2.3.2). Additionally, we set up a model with homogeneous K and perform the same experiments. The optimal K-value of the homogeneous model is chosen by minimizing the cumulative RMS-misfit when comparing these hypothetical pressure response curves with those of the Bolstern data set ("benchmarking"). We consider the value for K producing the smallest misfit to be the effective hydraulic conductivity K_{eff} and found the following value for the Bolstern aquifer analog:

$$K_{eff} = 7 \cdot 10^{-5} \, \frac{\mathrm{m}}{\mathrm{s}}.\tag{14}$$

In practice, K_{eff} may be inferred from the transmissivity that is estimated by conducting a single standard pumping test at the site.

We suggest two different approaches to use K_{eff} for calibrating the IP inversion results: (i) calibration with a constant factor (factor calibration) and (ii) calibration with a flexible calibration matrix using an exponential relationship (exponential calibration).

The first option consists of a simple multiplication of the inversion result K_{IP} with the calibration coefficient C, so that the geometric mean of the calibration result K_{fac} will be equal to K_{eff} :

$$\mathbf{K}_{\mathbf{fac}} = \mathbf{K}_{\mathbf{IP}} \cdot C,\tag{15}$$

$$C = \frac{K_{eff}}{mean(\mathbf{K_{IP}})}. (16)$$

This calibration is based on the assumption that K_{eff} should be close to the geometric mean of the K-values of the original data set K_{orig} (considering only the inner part between the boreholes), which for the Bolstern aquifer analog is found to be

$$mean(\mathbf{K_{orig}}) = 3.75 \cdot 10^{-5} \frac{\text{m}}{\text{s}}.$$
 (17)

 K_{eff} is slightly higher than this value, because it is typically more sensitive to the preferential flow paths (and therefore to areas with high K), especially in a highly anisotropic medium with pronounced horizontal layering as present in the Bolstern aquifer. However, we would still propose using the geometric mean of the K-field since this does not require any a priori assumptions about structural features or anisotropy in a field setting.

The exponential calibration attempts taking into account the different sensitivities of IP experiments and pumping tests by introducing a flexible calibration matrix \mathbf{C}_a . The concept of this approach is visualized in Appendix A, already including the results for different parameterizations. The calibration matrix is made up by

$$\mathbf{C}_{\alpha} = e^{\alpha \cdot \mathbf{K}_{\mathbf{IP}}} \tag{18}$$

and the calibration result K_{exp} is achieved by computing the Hadamard product between C_{α} and the inversion result K_{IP} :

$$\mathbf{K}_{\mathbf{exp}} = \mathbf{C}_{\alpha} \circ \mathbf{K}_{\mathbf{IP}}.\tag{19}$$

For low K-values (strong IP effect), the elements in \mathbf{C}_{α} will be close to one, so that the inversion result is not changed by the calibration, whereas for higher K-values (weak IP effect) the impact of the calibration generally becomes stronger. However, the overall strength and direction of the calibration is determined by the exponent α , which is chosen according to the pumping test data. We iterate over a wide range of values for α in order to minimize the misfit between the geometric mean of the calibration result $\mathbf{K}_{\mathrm{exp}}$ and K_{eff} .

$$\left| mean \left(\left[\mathbf{K}_{\mathbf{exp}} \right]_{\xi}^{100\%} \right) - K_{eff} \right| \xrightarrow{\alpha \in \mathbb{R}} min!$$
 (20)

Since K_{eff} is often higher than the actual geometric mean of K(as shown above for the Bolstern aquifer), we do not use the whole data set to compute the geometric mean within this calibration, but neglect a certain percentile ξ with the lowest *K*-values. The impact of ξ is visualized in Appendix A: for very low values (close to 0%) the result is likely to be over-corrected, whereas for too high values an undercorrection will occur. However, we find that the optimal percentile ξ can be estimated by visual assessment of the uncalibrated inversion result, and the function $\alpha(\xi)$ as shown in part (b) of Appendix A allows for an evaluation of the impact of different ξ -values on the calibration result. Typically, the optimal value for ξ will rise with increasing electrode spacing since smoothing effects lead to more extensive areas of low K. We finally choose $\xi = 30\%$ for 0.25 m spacing, $\xi = 35\%$ for 0.5 m spacing and $\xi = 50\%$ for 1 m spacing. Undoubtedly, this choice is to some extent subjective, and more experience and testing will be needed to choose the best value for ξ in other applications.

2.3. Hydraulic tomography

2.3.1. General concept

Hydraulic tomography (HT) requires hydraulic stimulation (e.g., pumping or slug tests) with several observation points at different locations to generate a tomographical configuration, similar to many geophysical tomography methods (Fig. 3b). The pressure response measured at the observation point is used to invert the stratigraphic structure, i.e. the spatial distribution of hydraulic diffusivity, hydraulic conductivity and specific storage. The main inversion algorithms consist

of geostatistics-based and travel time-based methods. The geostatistical methods for HT inversions can be predicated on a variety of algorithms, including simultaneous successive linear estimator (Berg and Illman, 2011; Yeh and Liu, 2000), quasi-linear estimator (Cardiff et al., 2020; Kitanidis, 1995) or ensemble Kalman filter (Sánchez-León et al., 2020). A common feature of these approaches is that they require a priori geostatistical models to assume the spatial correlation of the hydraulic parameters. In contrast, travel time methods used for HT inversion (Brauchler et al., 2003, 2013a) are based on an eikonal equation, which is transferred from the groundwater flow equation (Vasco et al., 2000) and can be solved by ray-tracing or particle tracking techniques. Compared to the first class of methods, this approach requires much less computational effort since it does not simulate in a complete groundwater flow model. Additionally, it does not require any prior assumptions about the geostatistical model, which can be highly uncertain due to the sparse measurements and various application scales. However, the travel time-based approach has limitations in reproducing the hydraulic parameters in low-permeability areas due to the low ray coverage. Although many studies prove that the structure of the formation can be readily reconstructed, a sequential inversion scheme is still required for a more accurate quantification of the hydraulic parameters (Hu et al., 2015, 2011; Jimenez et al., 2013).

2.3.2. Forward modeling

The synthetic HT experiments were simulated using the software Feflow (Diersch, 2014). The model domain was discretized by irregular triangular meshing. The initial hydraulic head in the whole domain is set to zero and we apply constant-head boundaries at the two sides. The hydraulic conductivity values were assigned to the mesh according to the values of the Bolstern aquifer analog, whereas the specific storage coefficient was assumed to be homogeneous at $S_s = 10^{-4} \text{ m}^{-1}$ according to typical values found in literature (Kuang et al., 2020). Source points were placed at the hypothetical borehole at x = 3 m, whereas receiver points were placed at x = 6 m and x = 9 m. Three different scenarios were simulated with varying vertical spacing of respectively 0.25 m, 0.5 m and 1 m within the boreholes. Therefore, the setups are similar to the IP experiments and the quality of the results can be directly compared. At the receiver points, the hydraulic head was recorded during the pumping tests, which are sequentially carried out from top to bottom. The pumping signal is a Heaviside function with a constant rate of 1 l/s, as shown in Fig. 3e.

The resulting pressure response curves were imported to Matlab for further processing. All source–receiver-combinations with a ray path angle larger than 60° were filtered out since the layered stratigraphy typical for a shallow porous medium can be better resolved by reducing those large-angle ray paths (Brauchler et al., 2007). The 10% diagnostic (Brauchler et al., 2003) is selected for the inversion, meaning that the early time $t_{\alpha,h}$ is picked where the derivative value reached 10% of the maximum derivative at the observation point (Fig. 3f). Hence, the data space consists of all source and receiver coordinates (except the filtered ones) as well as the respective early times. The travel time information was contaminated with a noise level of 3%, similar to Doetsch et al. (2010) and Hu et al. (2017).

2.3.3. Inversion

Hydraulic travel time of a pumping test is defined as a line integral in which the pumping-induced pressure is generated at the source point x_1 and travels along the path ε before reaching the receiver point x_2 :

$$\sqrt{t_{\alpha,h}} = \frac{1}{\sqrt{6f_{\alpha,h}}} \int_{x_1}^{x_2} \frac{d\varepsilon}{\sqrt{D(\varepsilon)}},\tag{21}$$

where $t_{\alpha,h}$ is the early time and $f_{\alpha,h}$ is a conversion factor (Brauchler et al., 2003). The subscript $_h$ indicates the usage of a Heaviside source. Similar to the seismic travel time inversion, Eq. (21) is resolved using ray tracing techniques, and the inverted slowness can be converted to the hydraulic diffusivity D. In this study, the open-source framework

pyGIMLi is utilized to invert the hydraulic travel times, which is based on the generalized Gauss–Newton method (Rücker et al., 2017; Günther et al., 2006) and where the forward operator for calculating the travel times uses Dijkstra's algorithm (Dijkstra, 1959). As a final step, we use the factor calibration approach introduced for IP to translate the achieved diffusivities **D** to a hydraulic conductivity distribution \mathbf{K}_{HT} that is in agreement with K_{eff} . This procedure replaces the common approach of multiplying with a specific storage coefficient S_s ($K = D \cdot S_s$), which is typically also assumed as homogeneous.

2.4. Tracer experiments

We want to assess the quality of the inversion results by performing synthetic tracer experiments using the achieved *K*-images and compare the results to those obtained by modeling with the original Bolstern data set.

The corresponding simulations were conducted using Feflow in the area between the hypothetical boreholes ($x = 3 \text{ m} \dots 9 \text{ m}$). Steady-state hydraulic conditions were assumed, and constant heads assigned to the model boundaries induce a hydraulic gradient of 0.001 between the inflow and outflow borders. A conservative tracer was injected as a hypothetical line source with a constant rate of 1 mg/l at the upstream border of the model domain (x = 3 m, left borehole). The longitudinal and vertical transverse dispersivities were set to $2.5 \cdot 10^{-2} \text{ m}$ and $2.5 \cdot 10^{-4} \text{ m}$, respectively, according to the values given in Höyng et al. (2015).

3. Results

3.1. HT and IP inversion results

Fig. 4c gives an overview of all the inversion results for the different methods and spacings. The original Bolstern data set is given at the top (Fig. 4a), where the grey numbers (1)–(5) indicate the most important highly permeable layers. Those layers are only subjectively defined to make it easier to refer to certain features in the text, but we will also show that they are responsible for the major tracer fingers found in the transport simulation presented below. Also note that the K-images derived from HT comprise only the domain between the boreholes (between x=3 m and x=9 m), whereas IP has the ability to image areas left and right of that domain as well, although with decreasing sensitivity. We show all the inversion results as images of K to allow a direct comparison.

The HT travel time inversion produced meaningful results that reveal the most important structures and overall good estimates of K. With 0.25 m and 0.5 m spacing, all the highly permeable layers (1)–(5) can be reconstructed at the correct locations and with well-estimated K-values. However, smaller heterogeneities, as e.g., within layer (2), cannot be resolved and some inversion artifacts are visible in the results, as e.g., a decrease in K in the direct vicinity of the left borehole. The inversion result for 1 m spacing misses the uppermost layer (1) since no source and receiver locations are present in this part of the aquifer. However, the other layers (2)–(5) are still visible, although smoothing effects are becoming more pronounced.

The travel time inversion typically yields integrated values along the different ray paths, which in our case produces an offset between *K*-values left and right of the central borehole. Although the general trend of the major layers is correct and the inversion results reflect the true behavior of the original data set, local *K*-heterogeneities are not always attributed to the exact location, but are smeared along the respective section of the ray path, creating a sharp border at the central borehole.

For IP we show the uncalibrated results for K as well as the images achieved by the new factor calibration and exponential calibration procedures. Note that the ThyCD inversion of IP data always yields a set of parameters, of which only K is shown in Fig. 4. An example of the complete set of parameters is given in Appendix B.

Firstly, we focus on the uncalibrated IP results. With 0.25 m electrode spacing, the aquifer heterogeneities are correctly reconstructed in terms of structural behavior and K-quantification. The highly permeable layers (1) - (4) are clearly retrieved by the inversion, but layer (5) can hardly be reproduced. Obviously, the sensitivity in this lowest part is small due to a very limited number of quadrupoles. However, when it comes to resolving smaller heterogeneities within the layers, IP yields slightly better results than HT and the attribution of certain K-heterogeneities to their exact location is more reliable.

When increasing the electrode spacing, smoothing effects introduced by the regularization become more pronounced and this effect is much stronger compared to the HT results. During IP measurements, one quadrupole integrates over an area of at least three times the spacing also in vertical direction, whereas for HT the integrative behavior is mainly related to the horizontal direction (along the ray path). Therefore, HT can resolve the borders between horizontal layers quite well, while this becomes much more difficult for IP. Another effect of the regularization is that the *K*-values, especially in the highly permeable layers, are typically under-estimated for larger electrode spacing. Therefore, we cannot expect to achieve correct transport simulations using those results. This can be overcome by using the new calibration procedures employed in the following.

The factor calibration leads to an overall increase in K for all three spacings since the value for K_{eff} is higher than the geometric mean of the inversion results. This yields an improvement in K-estimation especially for the larger spacings (0.5 m and 1 m), where the K-values of the most permeable layers are now predicted more correctly. However, an over-estimation of K can be observed in the less permeable zones. This drawback can be overcome by the exponential calibration, which leaves the lowest K-values unchanged and only adjusts the permeable zones to the pumping test data, as described in Section 2.2.4. This effect is clearly visible in the results: now the K-estimates are very close to the original data set in all parts of the aquifer and for all three spacings. The exponential calibration typically sharpens the contrast of the resulting image, thereby diminishing the smoothing effects especially for larger electrode spacings.

To quantify the reproduction quality of aquifer structures, we calculate the structural similarity index (SSIM) for each inversion result compared to the original data set (Fig. 4b). This metric is commonly used in image processing and measures the similarity between two images by taking into account luminance, contrast and structural information (Wang et al., 2004). It is bounded between 0 and 1, while the latter value indicates perfect similarity. We use the Python package "scikit-image" (van der Walt et al., 2014) to calculate the SSIM and find it to be a useful measure to assess the quality of the inversion results.

For all methods, a decreasing SSIM with increasing spacing can be observed due to lower data density and stronger smoothing effects. This behavior is expected and corresponds to the visual assessment of the inversion results. Generally, the lowest SSIM is computed for the HT results (between 0.17 and 0.05). Although the major layers are retrieved correctly, the method is not capable of retrieving the true structural behavior on smaller scales. The IP results yield relatively high SSIM values for the smallest spacing (0.30), indicating a good reproduction of the structural features. However, increasing the electrode spacing leads to a stronger decline of the SSIM compared to HT, showing again that smoothing effects are more pronounced for IP in this example. The factor calibration can strongly improve the structural reproduction, with the SSIM slightly increasing for 0.25 m spacing and strongly increasing for 0.5 m and 1 m spacing. While measurements with small spacing and therefore high data density cannot be improved much further by the calibration, the results achieved with larger spacing strongly benefit from this procedure. The exponential calibration is less successful in improving the structural information of the results, but still yields higher SSIM values compared to the uncalibrated IP tomograms.

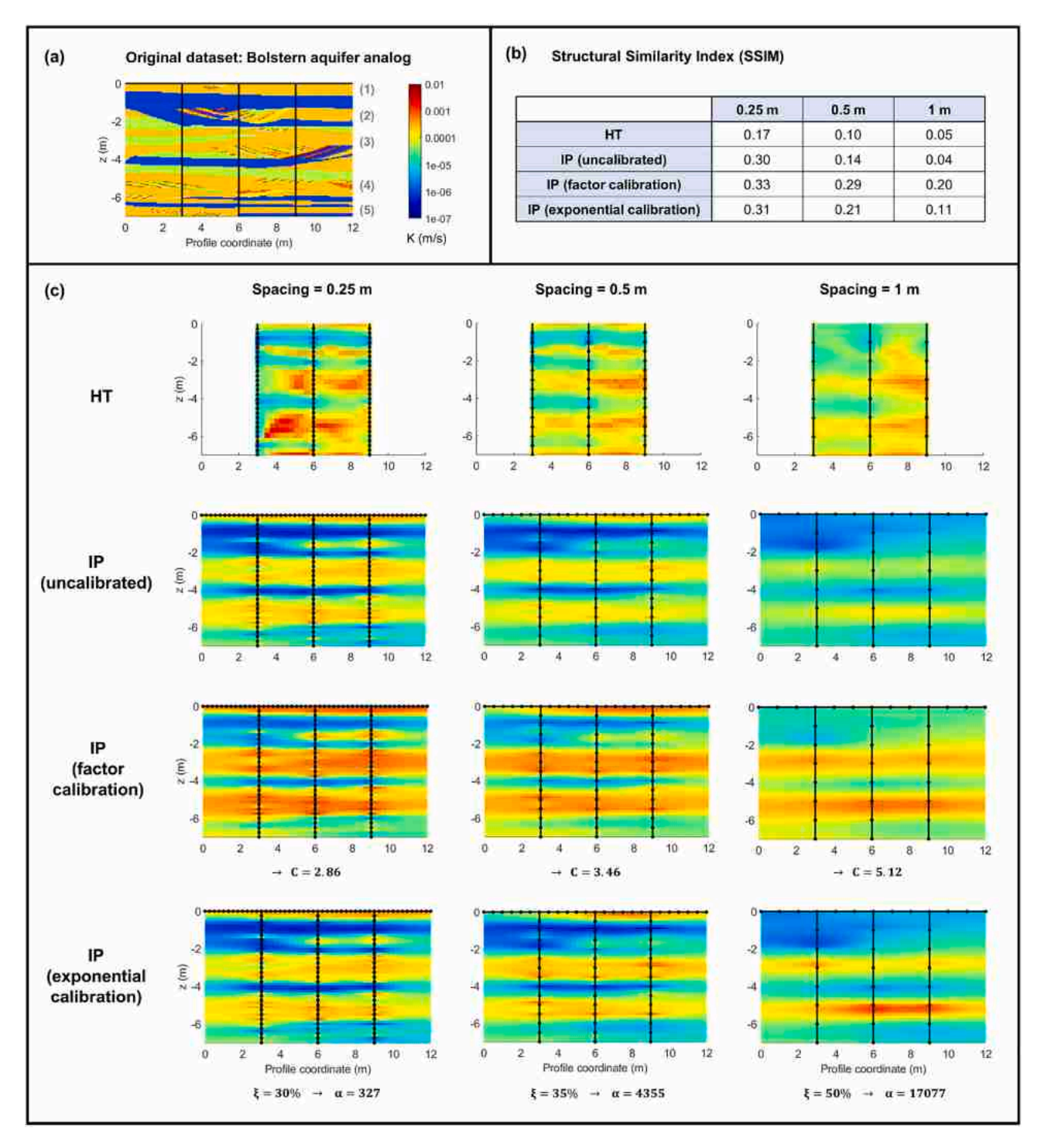


Fig. 4. (a) The original data set of the Bolstern aquifer analog. The colorbar for K also applies to all inversion results. (b) Structural similarity index (SSIM) of the inversion results compared to the original data set. (c) Overview of all inversion results for HT, IP and the two different IP calibrations for varying spacing of pumping locations/electrodes, given as images of K.

To further evaluate the prediction quality of the K-estimates, we show histograms of the ratio between the estimated and the true value for each cell of the inversion result (Fig. 5). To perform the comparison, the values of the 0.05 m \times 0.05 m cells of the original data set had to be averaged within the corresponding bigger cells of the inversion results. In the histograms, values at 10^0 indicate a perfect prediction of K compared to the averaged value of the original data set. We also

show the median value of the ratio (blue line) as well as how much of the prediction is within one order of magnitude (black lines and corresponding percentage) and within two orders of magnitude (red lines and corresponding percentage).

For the HT results a relatively broad distribution of prediction quality can be observed with approximately 90% of the values being within the 10^2 -interval and between 67% and 75% within the 10^1 -interval.

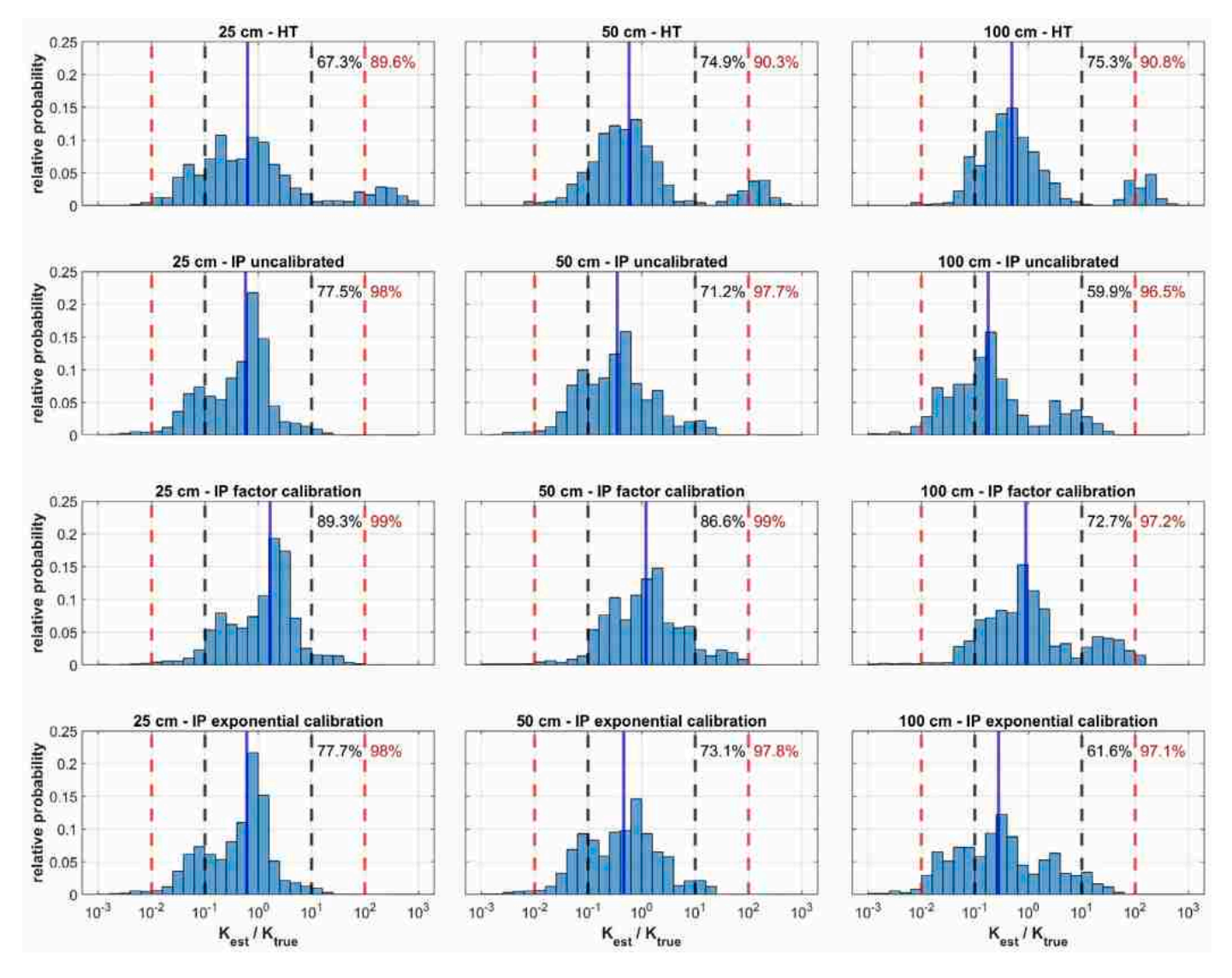


Fig. 5. Histograms of K_{est}/K_{true} (deviation of the inversion result from the true K-value for each cell) for the different methods, calibrations and spacings with the positions of the diagrams according to Fig. 4. The blue vertical lines indicate the median value (ideally at $10^0 = \text{no}$ deviation). The black (red) dashed lines show the one-(two-)order-of-magnitude-interval and the percentage indicates how many cells are within this range of deviation.

A significant number of cells is strongly over-estimated, leading to a slightly bimodal distribution of the investigated ratio with a smaller second maximum around 10^2 . The median value is slightly smaller than 10^0 for all three spacings.

The uncalibrated IP results show a narrower distribution of prediction quality with 96.5%–98% of the values within the 10^2 -interval. While the median value is close to 10^0 for the smallest electrode spacing, it is shifted to lower values with increasing spacing. At the same time, the percentage of values within the 10^1 -interval decreases from 77.5% to 59.9%. Due to the low data density and strong regularization effects, a majority of the K-values gets significantly under-estimated with increasing spacing.

After performing the factor calibration this bias produced by the inversion is mostly corrected with all median values being very close to 10^0 and a much higher number of values can be found within the 10^1 -interval. However, the growing range of the distribution with increasing spacing cannot be removed by the calibration. The exponential calibration improves the prediction quality compared to the uncalibrated results, but is less successful than the factor calibration.

In the same way, a possible bias of the petrophysical laws underlying the inversion procedure might be corrected by the suggested calibration approaches. While the IP method is very well capable of retrieving the structural information correctly and giving a rough estimation of the expected trend in the K-values, the calibration using hydraulic information is being used for a more exact K-estimation. Still, it is important to note that the inherent scatter of the petrophysical laws cannot be removed and the achieved K-distribution remains an approximation of the reality within the limits of the accuracy of the petrophysical relations.

3.2. Transport simulation

3.2.1. Snapshots of tracer plumes

Firstly, we evaluate the results of the transport modeling by imaging the tracer plumes that are simulated using the different inversion results as input data for the K-distribution. Fig. 6 shows an overview of snapshots taken at a simulation time of 50 days after starting the tracer injection for the different methods and calibrations as well as point

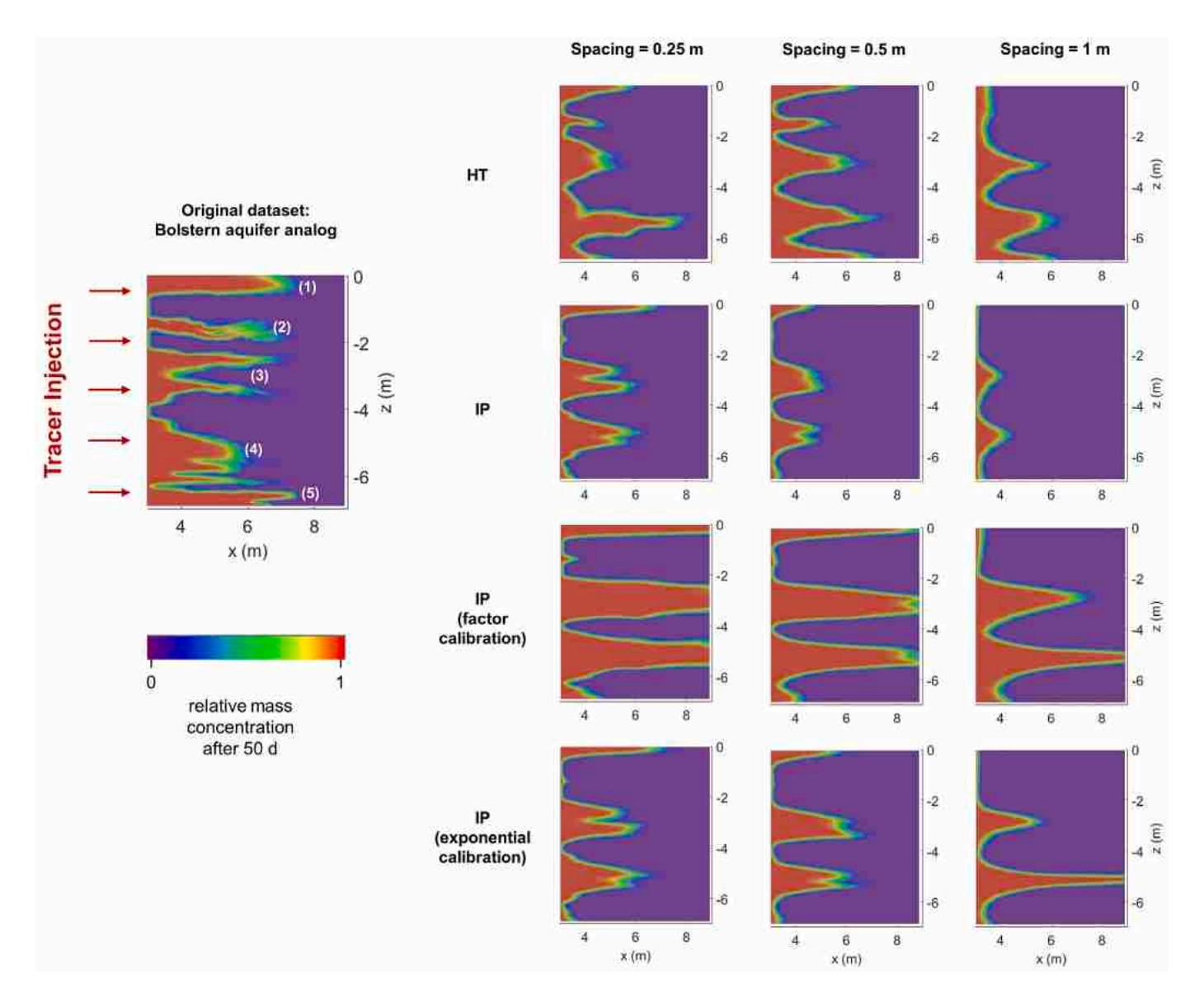


Fig. 6. Transport modeling results for HT, IP and the two different IP calibrations for varying spacing of pumping locations/electrodes, given as images of relative mass concentration of the tracer injected in the left borehole. The result for the original data set of the Bolstern aquifer analog is given on the left for comparison. Here, the numbers (1)–(5) indicate the preferential flow paths identified in Fig. 4. All the plots show snapshots taken 50 days after starting the tracer injection. The same color bar applies to all images.

spacings, arranged similarly to Fig. 4. The result for the original data set is given on the left side and we consider this to be the actual tracer concentration that would be observed in reality as a basis for comparison. The highly permeable zones (1)–(5) identified in Fig. 4 have produced fingering tracer plumes, that mostly extend as far as the center part of the domain ($x = 6 \dots 7$ m). Finger (2) inhibits some smaller variations due to the small-scale K-heterogeneities and finger (3) splits up into two thinner layers with high tracer concentration.

The HT results for 0.25 m and 0.5 m spacing correctly show all tracer fingers (1)–(5) with roughly the right extension and shape. Smaller features, as e.g., the variations in finger (2) or the splitting of finger (3), however, can hardly be made out. With 1 m spacing the two uppermost tracer fingers disappeared due to smoothing effects and the lack of pumping locations at the very top and only the fingers (3), (4) and (5) are modeled correctly.

Using the IP inversion results for the tracer prediction correctly reproduces the fingers (1), (3) and (4) with the right extension and shape. Some small-scale features, like the splitting of finger (3), are

more realistic compared to HT. However, finger (2) gets strongly underestimated due to smoothing effects, and layer (5) cannot be sensed due to the lack of quadrupoles in the lowest part of the domain. With larger spacing, the stronger influence of the smoothing effects becomes apparent. The simulation with 1 m spacing can only reproduce the fingers (3) and (4), but they do not extend as far as they should. This indicates, that for cross-hole IP measurements a small enough electrode spacing is crucial to obtain reliable results.

The tracer prediction resulting from the factor calibration shows a clear over-estimation of K in the highly permeable layers with the fingers (1), (3) and (4) extending too far to the right. This effect is strongest for 0.25 m spacing, where the plume is already extending out of the domain at this time step. For the larger spacings, the images are at least closer to the reality than the uncalibrated results, although still somewhat over-corrected.

The best prediction of tracer plumes is achieved by the exponential calibration. For 0.25 m spacing the uncalibrated result has already been close to reality and it remains almost unchanged by the exponential

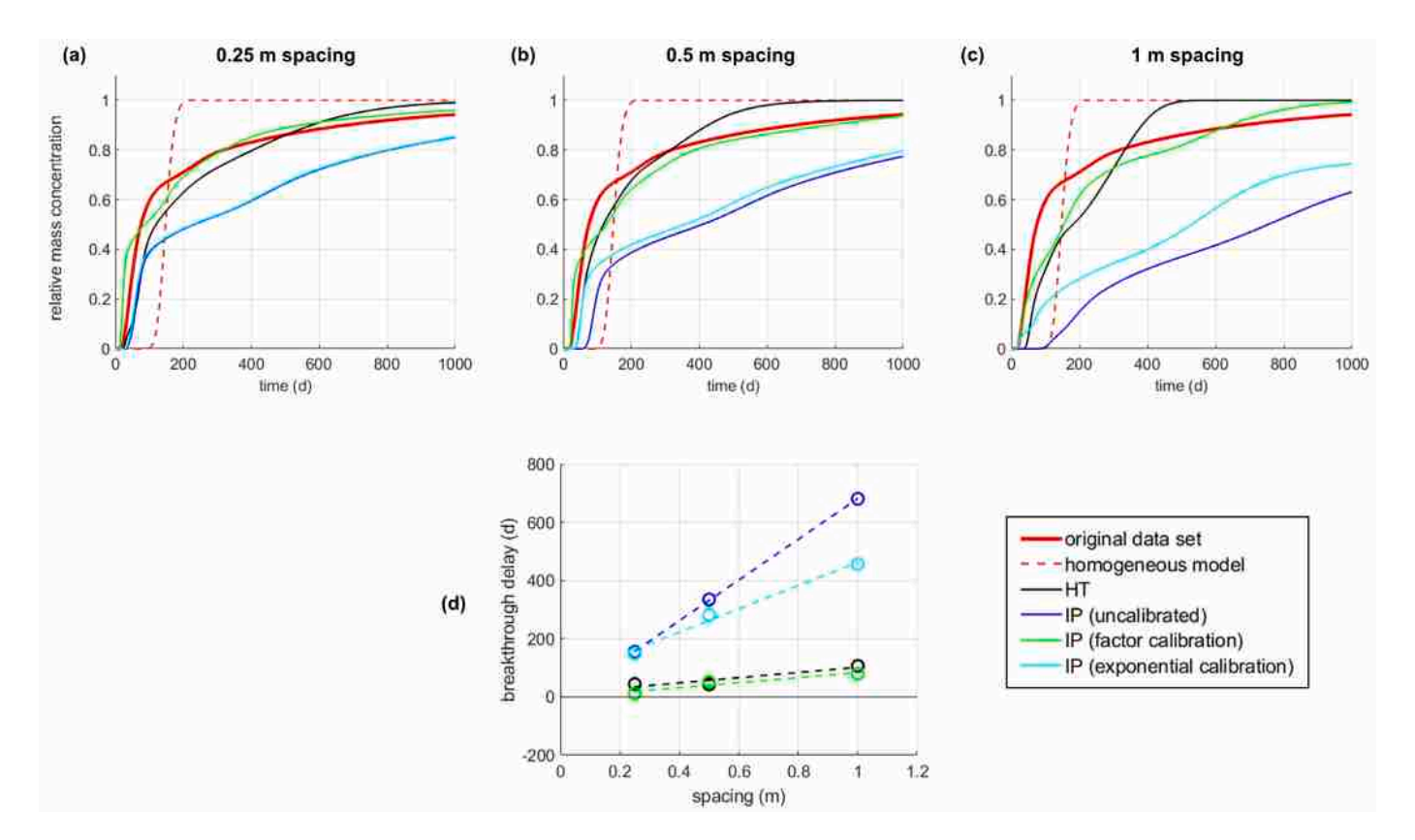


Fig. 7. (a)–(c): Depth-integrated tracer breakthrough curves at the center borehole (x = 6 m) resulting from different inversion results and calibrations compared to the original Bolstern data set (red solid line) and a hypothetical homogeneous model (red dashed line) for varying spacing of pumping locations/electrodes. (d) Breakthrough delay of the different methods and calibrations depending on the varying point spacing as a measure for the error of the transport simulations compared to the original data set. The dashed lines represent a linear regression between the data points for visual guidance only.

calibration. A stronger effect of the calibration is visible for 0.5 m spacing, where the extension of the plumes is now predicted correctly. For 1 m spacing the result is still quite far from reality since the calibration cannot compensate for the lack in identified structures and the strong smoothing effects. Even so, there is a clear improvement compared to the uncalibrated result.

3.2.2. Tracer breakthrough curves

The depth-integrated relative tracer concentration over time at the central borehole (x = 6 m) is depicted in Fig. 7a–c. The concentrations were also recorded in the right borehole (x = 9 m), but all the main trends in the results are similar, so they are not further detailed here.

The breakthrough curve (BTC) for the original data set (red line) shows a relatively steep increase in tracer concentration within the first 150 days, which is stimulated by the highly permeable layers in the aquifer (layers (1)–(5) in Figs. 4 and 6). For later times, we observe a much slower increase in concentration as a result of the delayed propagation in the less permeable parts.

As a basis for comparison, we also show the BTC of a hypothetical homogeneous model with $K_{eff}=7\cdot 10^{-5}~{\rm m~s^{-1}}$ (red, dashed line). Here, we only observe a relatively quick incline of tracer concentration in the time span between 150 and 200 days. However, the true shape of the BTC cannot be reproduced, since no structural information on the sediments is processed. In contrast, all transport simulation results from HT and IP better approximate the true shape of the BTC. Apparently, the structural information gained from the two imaging techniques is valuable, even when just looking at depth-integrated BTCs. Especially the tracer breakthrough at early times is strongly under-estimated by the homogeneous model.

The HT results (black lines) are successful in reproducing the whole BTC, although we observe a slight under-estimation of tracer breakthrough at early times and an over-estimation at late times. This

can be interpreted as a result of smoothing effects, leading to a less pronounced distinction between areas with higher or lower K. It corresponds with the fact that this effect becomes stronger with increasing spacing, where smoothing effects have more impact.

Although the IP results (dark blue lines) correctly reproduce the general shape of the BTC (due to correctly retrieved structural information), they strongly under-estimate the tracer breakthrough within the entire time span. Apparently, the tomograms are not accurate enough to be used for a transport simulation.

The exponential calibration (cyan lines) mainly corrects the early-time behavior of the BTC since only the highly permeable parts are changed by this calibration approach. Especially for the larger spacings (0.5 m and 1 m) this brings an advantage compared to the uncalibrated result, whereas for the smallest spacing (0.25 m) almost no change can be observed. This is in agreement with the findings for the inversion results (Fig. 4) and the tracer plumes (Fig. 6). For the late times, the calibration does not compensate the under-estimation of tracer breakthrough. However, this is not caused by an under-estimation of K in the less permeable zones, since the slope of the BTC is correctly reproduced. Instead, the extension of high-K-zones is underestimated due to regularization (especially for large spacings) and therefore the early-time breakthrough reaches lower concentrations. This offset remains for the whole time span and leads to an overall under-prediction of tracer breakthrough.

The factor calibration (green lines) is more successful in correcting the IP results. Although the tracer concentration is over-estimated for early times, the long-term behavior is correctly predicted with a quality that is at least similar to the HT results. Applying the K_{eff} -value to the whole domain yields the best K-prediction in terms of average values and therefore the best reproduction of the complete BTC.

Finally, we assess the impact of the point spacing (electrodes or pumping locations) on the quality of the tracer breakthrough prediction. For this purpose, we pick a certain breakthrough time for all curves at the time where half of the relative concentration has been reached. We calculate the difference to the breakthrough time of the original data set and call this the breakthrough delay, considering it a rough measure for the error in the prediction of the BTC. The dependency of the delay on the spacing is shown in Fig. 7d. For all methods we observe an increase of the delay for increasing spacing due to a lower data density and stronger smoothing effects. This effect is only weakly pronounced for the HT results, indicating again that the point spacing is not as crucial and relatively good results can also be achieved with fewer pumping tests. On the other hand, the dependency on electrode spacing of the uncalibrated IP results is very pronounced, showing that a sufficiently small electrode spacing is particularly important to retrieve all the necessary structural information and gain good K-estimates. However, acquiring cross-borehole IP data with such small spacing in the field can be a very challenging task. Therefore, we consider the calibration with hydraulic data to be valuable especially when a larger spacing has to be used and therefore important structural information is not well resolved. While the exponential calibration can only slightly compensate for those problems, the factor calibration is very successful in reducing the breakthrough delay. Here, the results have a quality very similar to the HT data and the errors resulting from the large electrode spacing have been reduced significantly.

4. Conclusions

We have shown that both HT and IP are valuable tools for imaging K-heterogeneities in near-surface aquifers. The structural information of our test data set, the Bolstern aquifer analog, has been reconstructed by the inversion procedures to a high degree of resolution and quantitative accuracy. For the first time, the distribution of K could be computed directly from the IP data with our new IP-K inversion procedure and the general quality of the results is comparable to the HT travel time inversion. However, to achieve highly accurate K-estimates that allow using the results for groundwater modeling, we calibrate the results with hydraulic information. After the factor calibration, the depth-integrated tracer BTCs of the original data set could be reproduced. Imposing K_{eff} on the whole domain leads to a good prediction of the long-term behavior of tracer breakthrough. On the other hand, the exponential calibration is more suitable to correctly predict the tracer plumes at early times. Therefore, in practice it would be necessary to decide on one of the calibrations depending on how the data will be used later on. Both calibrations may not only correct regularization-induced errors in K-prediction, but also a possible bias of the petrophysical laws that link electrical and hydrological parameters. Although we cannot account for the inherent scatter of the petrophysical relations, we still consider those calibrations to be highly valuable tools within the processing of IP data. While the structural features of an aquifer can be accurately retrieved with IP, hydraulic information is essential for a reliable K-quantification.

Future research should focus on testing the suggested methodology within field experiments. The new IP-K inversion procedure for IP data has already been tested on borehole data (Fiandaca et al., 2021) and 2D surface profiles from five different European countries (Martin et al., 2021), giving K-values within one decade from slug tests/grain size analysis estimates. However, no benchmarking of the field K-estimates for flow and transport modeling or tracer experiments have been conducted yet.

Ideally, future field experiments should follow a similar concept as presented in this study (Fig. 1). Conducting both HT and IP experiments at the same site would allow a direct comparison of the performance of the methods in the field. Furthermore, the pumping tests carried out for the HT survey could provide the K_{eff} -value needed for the IP

calibrations. Finally, the quality of the achieved K-images might also be tested by tracer experiments.

On the other hand, field campaigns with limited financial and time resources may now also rely on IP measurements alone (together with one or just a few pumping tests for retrieving K_{eff}) following the suggested calibration methodology. While a full HT experiment is often very time-consuming and costly, IP measurements can mostly be conducted within a few hours (in a setting similar to the example shown in this work). Therefore, a detailed characterization of aquifer heterogeneities in the field might become more convenient by applying our IP-K inversion procedure and the results can be expected to have a similar quality compared to HT.

However, the two calibration approaches suggested in this work should only be regarded as a starting point. In a real field environment, further elaborated calibration methods might turn out to be more successful. Furthermore, stronger data integration approaches between hydraulic and geophysical methods are expected to yield even better results. While hydraulic methods are often most sensitive to preferential flow paths, IP generates the strongest polarization response in areas of low K. We therefore see a big potential in using the complementary sensitivities of the two methods by a stronger integration of the data. Ultimately, a fully-joint inversion of HT and IP data sets might open the door to an improved ability of imaging hydraulic conductivity in near-surface aquifers.

CRediT authorship contribution statement

Lukas Römhild: Conceptualization, Methodology, Investigation, Data curation, Writing – original draft, Visualization. **Gianluca Fiandaca:** Conceptualization, Methodology, Software, Writing – review & editing, Supervision. **Linwei Hu:** Conceptualization, Methodology, Investigation, Writing – review & editing. **Laura Meyer:** Methodology, Investigation, Writing – review & editing. **Peter Bayer:** Conceptualization, Writing – review & editing, Supervision, Project administration.

Declaration of competing interest

The authors declare that they have no known competing financial interests or personal relationships that could have appeared to influence the work reported in this paper.

Data availability

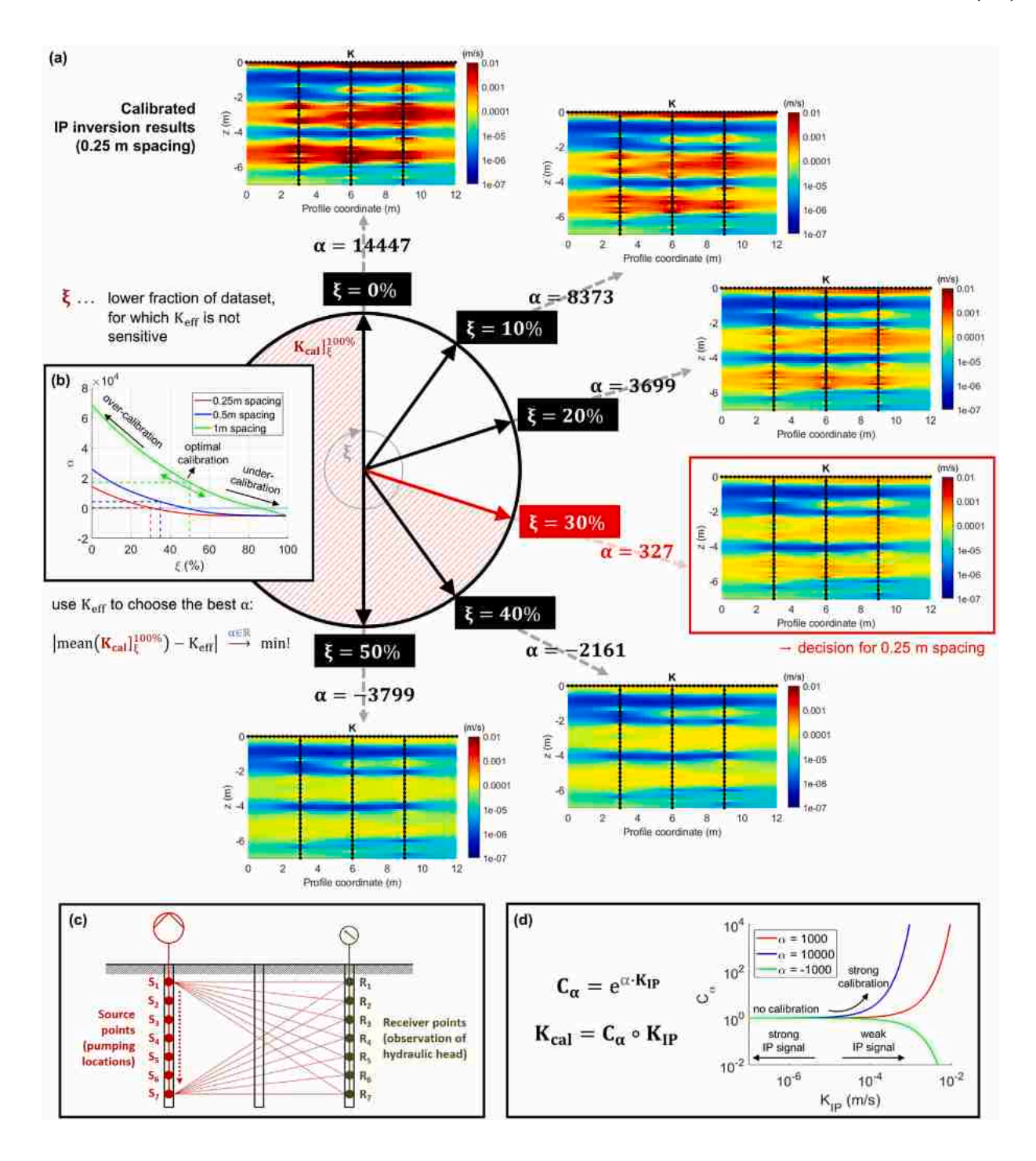
The original Bolstern data set as well as all HT and IP inversion results are available through https://doi.org/10.5281/zenodo.6361423.

Acknowledgments

This study is part of the project GeoPHydro – GeoPhysics for Hydrogeology, funded by A2A ciclo idrico, Italy. The authors would like to thank Andreas Weller for his valuable feedback on the petrophysical foundation of the IP inversion as well as Robin Thibaut for his advice on using the SSIM. Furthermore, we thank Thomas Hermans, Niklas Linde and one anonymous reviewer for their constructive comments that helped to improve the manuscript and Ryan Pearson for proofreading.

Appendix A. Strategy of the exponential calibration

Visualization of the concept of the exponential calibration of IP inversion results by incorporating pumping test data. (a) The selection of a suitable ξ -percentile influences the resulting value for α , thereby determining the overall strength and direction of the calibration. (b) The function $\alpha(\xi)$ for the three different spacings using $K_{eff} = 7 \cdot 10^{-5}$ m s⁻¹ as retrieved from the pumping test data. This plot is typically helpful to find a reasonable value for ξ . It should usually be higher for larger electrode spacings (e.g., green line - 1 m spacing) since smoothing

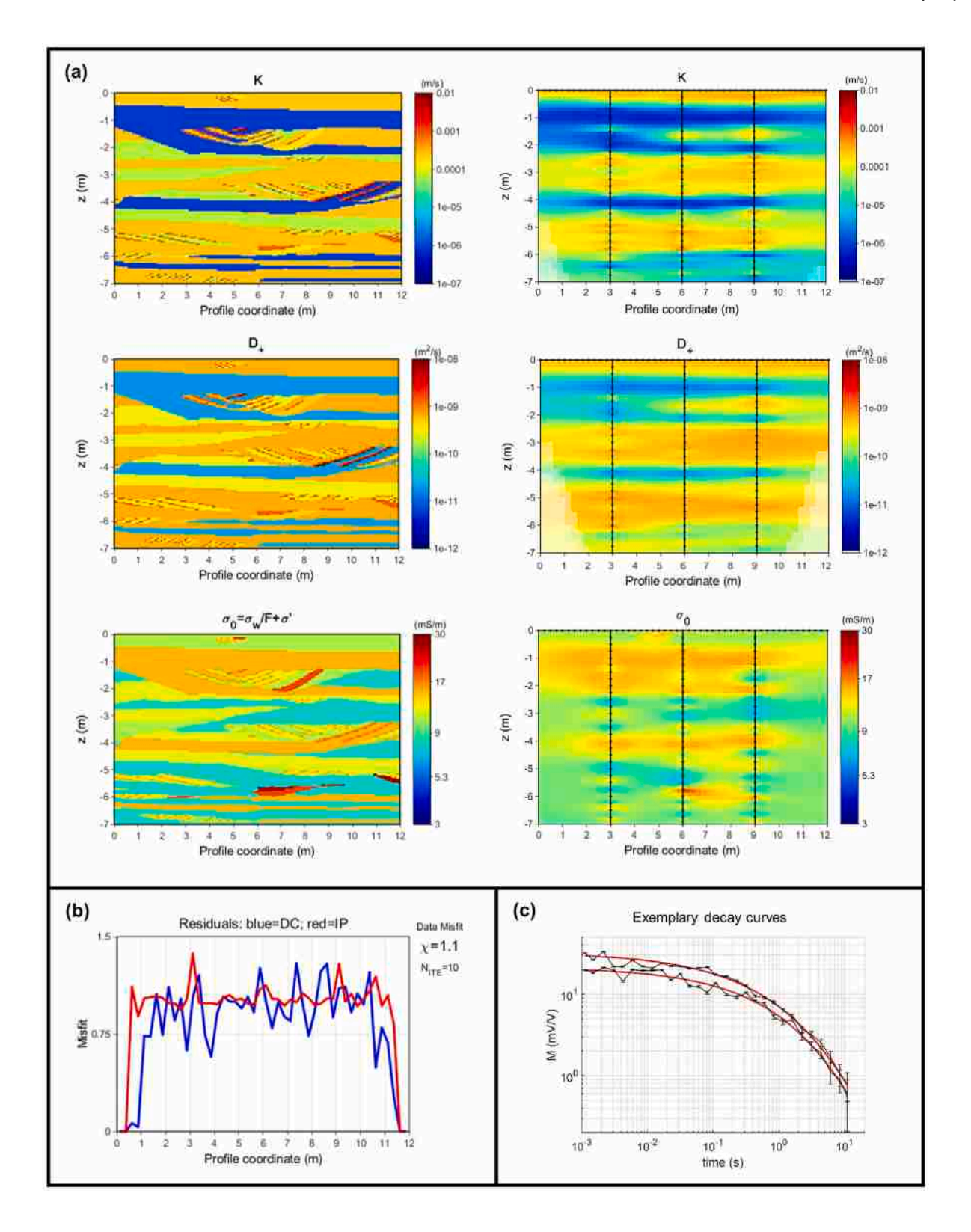


effects lead to more extensive areas of low K. (c) Setup of pumping tests for the derivation of K_{eff} . The source–receiver combinations used for this procedure are a subset of the full HT data set. (d) The dependence of C_{α} on the respective K-values of the inversion result, visualizing the exponential law inspired by the strength of the IP signal and the effect of different α -values.

Appendix B. Full forward model and IP inversion result

(a) Left part: Bolstern aquifer analog data including the parameters hydraulic conductivity K, diffusion coefficient D_+ and total electrical conductivity σ_0 as a combination of water conductivity σ_w , formation factor F and the real part of interface conductivity σ'_{int} . The frequency exponent c is assumed to be homogeneous and is therefore not shown

here. The forward modeling was performed in the WhyCDF model space. Right part: IP inversion result, performed in the ThyCD model space with 0.25 m electrode spacing. The transparent parts (lower corners) indicate areas with low sensitivity. **(b)** Misfit of the inversion result along the whole profile. The misfits of the DC data (blue line) and the IP data (red line) end up to be very balanced and the overall data misfit $\chi=1.1$ indicates that after the inversion the data are fitted closely to the noise level. The final result was achieved after ten iterations. **(c)** Exemplary decay curves of the forward simulation with added Gaussian noise (black lines) including error bars of the assumed standard deviation model and fitted decay curves of the inversion result (red lines).



References

Ahmed, A.S., Jardani, A., Revil, A., Dupont, J.P., 2016. Specific storage and hydraulic conductivity tomography through the joint inversion of hydraulic heads and self-potential data. Adv. Water Resour. 89, 80–90. http://dx.doi.org/10.1016/j.advwatres.2016.01.006.

Archie, G.E., 1942. The electrical resistivity log as an aid in determining some reservoir characteristics. Trans. Am. Inst. Min. Meall. Pet. Eng. 146, 54–62. $\frac{146}{1000}, \frac{146}{1000}, \frac{146}$ Attwa, M., Günther, T., 2013. Spectral induced polarization measurements for predicting the hydraulic conductivity in sandy aquifers. Hydrol. Earth Syst. Sci. 17, 4079–4094. http://dx.doi.org/10.5194/hess-17-4079-2013.

Benoit, S., Ghysels, G., Gommers, K., Hermans, T., Nguyen, F., Huysmans, M., 2019. Characterization of spatially variable riverbed hydraulic conductivityusing electrical resistivity tomography and induced polarization. Hydrogeol. J. 27, 396–407. http://dx.doi.org/10.1007/s10040-018-1862-7.

Berg, S.J., Illman, W.A., 2011. Three-dimensional transient hydraulic tomography in a highly heterogeneous glaciofluvial aquifer-aquitard system. Water Resour. Res. 47

- (10), http://dx.doi.org/10.1029/2011WR010616.
- Bing, Z., Greenhalgh, S.A., 2000. Cross-hole resistivity tomography using different electrode configurations. Geophys. Prospect. 48, 887–912. http://dx.doi.org/10. 1046/j.1365-2478.2000.00220.x.
- Binley, A., Hubbard, S.S., Huisman, J.A., Revil, A., Robinson, D.A., Singha, K., Slater, L., 2015. The emergence of hydrogeophysics for improved understanding of subsurface processes over multiple scales. Water Resour. Res. 51, 3837–3866. http://dx.doi. org/10.1002/2015WR017016.
- Binley, A., Keery, J., Slater, L., Barrash, W., Cardiff, M., 2016. The hydrogeological information in cross-borehole complex conductivity data from an unconsolidated conglomeratic sedimentary aquifer. Geophysics 91, E409–E421. http://dx.doi.org/ 10.1190/geo2015-0608.1.
- Binley, A., Slater, L.D., Fukes, M., Cassiani, G., 2005. Relationship between spectral induced polarization and hydraulic properties of saturated and unsaturated sandstone. Water Resour. Res. 41, W12417. http://dx.doi.org/10.1029/2005WR004202.
- Bohling, G.C., Butler, Jr., J.J., 2010. Inherent limitations of hydraulic tomography. Groundwater 48 (6), 809–824. http://dx.doi.org/10.1111/j.1745-6584.2010.00757.
- Bording, T.S., Fiandaca, G., Maurya, P.K., Auken, E., Christiansen, A.V., Tuxen, N., Klint, K.E.S., Larsen, T.H., 2019. Cross-borehole tomography with full-decay spectral time-domain induced polarization for mapping of potential contaminant flow-paths. J. Contam. Hydrol. 226, 103523. http://dx.doi.org/10.1016/j.jconhyd. 2019 103523
- Börner, J.H., Herdegen, V., Repke, J.U., Spitzer, K., 2017. Spectral induced polarization of the three-phase system CO2 brine sand under reservoir conditions. Geophys. J. Int. 208, 289–305. http://dx.doi.org/10.1093/gji/ggw389.
- Börner, F.D., Schopper, J.R., Weller, A., 1996. Evaluation of transport and storage properties in the soil and groundwater zone from induced polarization measurements. Geophys. Prospect. 44, 583–601. http://dx.doi.org/10.1111/j.1365-2478. 1996.tb00167.x.
- Brauchler, R., Böhm, G., Leven, C., Dietrich, P., Sauter, M., 2013a. A laboratory study for tracer tomography. Hydrogeol. J. 21, 1265–1274. http://dx.doi.org/10.1007/s10040-013-1006-z.
- Brauchler, R., Cheng, J.T., Dietrich, P., Everett, M., Johnson, B., Liedl, R., Sauter, M., 2007. An inversion strategy for hydraulic tomography: Coupling travel time and amplitude inversion. J. Hydrol. 345, 184–198. http://dx.doi.org/10.1016/j.jhydrol. 2007.08.011
- Brauchler, R., Hu, R., Hu, L., Jiménez, S., Bayer, P., Dietrich, P., Ptak, T., 2013b. Rapid field application of hydraulic tomography for resolving aquifer heterogeneity in unconsolidated sediments. Water Resour. Res. 49 (4), http://dx.doi.org/10.1002/wrcr.20181.
- Brauchler, R., Liedl, R., Dietrich, P., 2003. A travel time based hydraulic tomographic approach. Water Resour. Res. 39 (12), 1370. http://dx.doi.org/10.1029/2003WR002262.
- Cardiff, M., Barrash, W., Kitanidis, P.K., 2013. Hydraulic conductivity imaging from 3-D transient hydraulic tomography at several pumping/observation densities. Water Resour. Res. 49 (11), http://dx.doi.org/10.1002/wrcr.20519.
- Cardiff, M., Zhou, Y., Barrash, W., Kitanidis, P.K., 2020. Aquifer imaging with oscillatory hydraulic tomography: Application at the field scale. Groundwater 58 (5), 710–722. http://dx.doi.org/10.1111/gwat.12960.
- Cole, K.S., Cole, R.H., 1941. Dispersion and absorption in dielectrics I. Alternating current characteristics. J. Chem. Phys. 9, 341–351. http://dx.doi.org/10.1063/1. 1750906
- Diersch, H.J.G., 2014. FEFLOW Finite Element Modeling of Flow, Mass and Heat Transport in Porous and Fractured Media. Springer-Verlag Berlin Heidelberg.
- Dijkstra, E.W., 1959. A note on two problems in connexion with graphs. Numer. Math. 1 (1), 269–271.
- Doetsch, J., Fiandaca, G., Auken, E., Christiansen, A.V., Cahill, A.G., Jakobsen, R., 2015. Field-scale time-domain spectral induced polarization monitoring of geochemical changes induced by injected CO2 in a shallow aquifer. Geophysics 80 (2), 113–126. http://dx.doi.org/10.1190/GEO2014-0315.1.
- Doetsch, J., Linde, N., Binley, A., 2010. Structural joint inversion of time-lapse crosshole ERT and GPR traveltime data. Geophys. Res. Lett. 37 (24), http://dx.doi.org/10.1029/2010GL045482.
- Fiandaca, G., Auken, E., Christiansen, A.V., Gazoty, A., 2012. Time-domain-induced polarization: Full-decay forward modeling and 1D lateral constrained inversion of cole-cole parameters. Geophysics 77 (3), 213–225. http://dx.doi.org/10.1190/ GEO2011-0217.1.
- Fiandaca, G., Madsen, L.M., Maurya, P.K., 2018a. Re-parameterisations of the cole-cole model for improved spectral inversion of induced polarization data. Near Surf. Geophys. 16, 385–399. http://dx.doi.org/10.3997/1873-0604.2017065.
- Fiandaca, G., Madsen, L.M., Olmo, M., Römhild, L., Maurya, P., 2021. Inversion of hydraulic conductivity from induced polarisation, part a: Methodology and verification. In: NSG2021 1st Conference on Hydrogeophysics. http://dx.doi.org/ 10.3997/2214-4609.202120192.
- Fiandaca, G., Maurya, P.K., Balbarini, N., Hördt, A., Christiansen, A.V., Foged, N., Bjerg, P.L., Auken, E., 2018b. Permeability estimation directly from logging-whiledrilling induced polarization data. Water Resour. Res. 54, http://dx.doi.org/10. 1002/2017WR022411.

- Fiandaca, G., Ramm, J., Binley, A., Gazoty, A., Christiansen, A.V., Auken, E., 2013. Resolving spectral information from time domain induced polarization data through 2-D inversion. Geophys. J. Int. 192, 631–646. http://dx.doi.org/10.1093/gji/ cos/660
- Gallistl, J., Weigand, M., Stumvoll, M., Ottowitz, D., Glade, T., Orozco, A.F., 2018. Delineation of subsurface variability in clay-rich landslides through spectral induced polarization imaging and electromagnetic methods. Eng. Geol. 245, 292–308. http://dx.doi.org/10.1016/j.enggeo.2018.09.001.
- Gao, G., Abubaker, A., Habashy, T., 2012. Joint petrophysical inversion of electromagnetic and full-waveform seismic data. Geophysics 77 (3), WA3–WA18. http://dx.doi.org/10.1190/geo2011-0157.1.
- Gazoty, A., Fiandaca, G., Pedersen, J., Auken, E., Christiansen, A.V., Pedersen, J.K., 2012. Application of time domain induced polarization to the mapping of lithotypes in a landfill site. Hydrol. Earth Syst. Sci. 16, 1793–1804. http://dx.doi.org/10. 5194/hess-16-1793-2012.
- Gottlieb, J., Dietrich, P., 1995. Identification of the permeability distribution in soil by hydraulic tomography. Inverse Problems 11.2, 353.
- Günther, T., Rücker, C., Spitzer, K., 2006. Three-dimensional modelling and inversion of dc resistivity data incorporating topography II. Inversion. Geophys. J. Int. 166 (2), 506–517. http://dx.doi.org/10.1111/j.1365-246X.2006.03011.x.
- Heinz, J., Kleineidam, S., Teutsch, G., Aigner, T., 2003. Heterogeneity patterns of quaternary glaciofluvial gravel bodies (SW-Germany): application to hydrogeology. Sediment. Geol. 158, 1–23. http://dx.doi.org/10.1016/S0037-0738(02)00239-7.
- Hermans, T., Irving, J., 2017. Facies discrimination with electrical resistivity tomography using a probabilistic methodology: effect of sensitivity and regularisation. Near Surf. Geophys. 15, 13–25. http://dx.doi.org/10.3997/1873-0604.2016047.
- Hördt, A., Druiventak, A., Blaschek, R., Binot, F., Kemna, A., Kreye, P., Zisser, N., 2009. Case histories of hydraulic conductivity estimation with induced polarization at the field scale. Near Surf. Geophys. 7, 529–545. http://dx.doi.org/10.3997/1873-0604.2009035.
- Höyng, D., Prommer, H., Blum, P., Grathwohl, P., D'Affonseca, F.M., 2015. Evolution of carbon isotope signatures during reactive transport of hydrocarbons in heterogeneous aquifers. J. Contam. Hydrol. 174, 10–27. http://dx.doi.org/10.1016/ j.jconhyd.2014.12.005.
- Hu, L., Bayer, P., Alt-Epping, P., Tatomir, A., Sauter, M., Brauchler, R., 2015. Time-lapse pressure tomography for characterizing CO2 plume evolution in a deep saline aquifer. Int. J. Greenh. Gas Control 39, 91–106. http://dx.doi.org/10.1016/j.ijggc. 2015.04.013.
- Hu, R., Brauchler, R., Herold, M., Bayer, P., 2011. Hydraulic tomography analog outcrop study: Combining travel time and steady shape inversion. J. Hydrol. 409, 350–362. http://dx.doi.org/10.1016/j.jhydrol.2011.08.031.
- Hu, L., Doetsch, J., Brauchler, R., Bayer, P., 2017. Characterizing CO2 plumes in deep saline formations; comparison and joint evaluation of time-lapse pressure and seismic tomography. Geophysics 82 (4), 1–18. http://dx.doi.org/10.1190/ GEO2016-0365.1.
- Irving, J., Singha, K., 2010. Stochastic inversion of tracer test and electrical geophysical data to estimate hydraulic conductivities. Water Resour. Res. 46 (11), http://dx. doi.org/10.1029/2009WR008340.
- Jimenez, S., Brauchler, R., Bayer, P., 2013. A new sequential procedure for hydraulic tomographic inversion. Adv. Water Resour. 62, 59–70. http://dx.doi.org/10.1016/ j.advwatres.2013.10.002.
- Kenna, A., Binley, A., Cassiani, G., Niederleithinger, E., Revil, A., Slater, L., Williams, K.H., Orozco, A.F., Haegel, F.H., Hördt, A., Kruschwitz, S., Leroux, V., Titov, K., Zimmermann, E., 2012. An overview of the spectral induced polarization method for near-surface applications. Near Surf. Geophys. 10, 453–468. http://dx.doi.org/10.3997/1873-0604.2012027.
- Kemna, A., Binley, A., Slater, L., 2004. Crosshole IP imaging for engineering and environmental applications. Geophysics 69 (1), 97–107. http://dx.doi.org/10.1190/ 1.1649379.
- Kitanidis, P., 1995. Quasi-linear geostatistical theory for inversing. Water Resour. Res. 31 (10), 2411–2419. http://dx.doi.org/10.1029/95WR01945.
- Klepikova, M., Brixel, B., Jalali, M., 2020. Transient hydraulic tomography approach to characterize main flowpaths and their connectivity in fractured media. Adv. Water Resour. 136, 103500. http://dx.doi.org/10.1016/j.advwatres.2019.103500.
- Kong, X.Z., Deuber, C.A., Kittilä, A., Somogyvari, M., Mikutis, G., Bayer, P., Stark, W.J., Saar, M.O., 2018. Tomographic reservoir imaging with DNA-labeled silica nanotracers: The first field validation. Environ. Sci. Technol. 52 (23), 13681–13689. http://dx.doi.org/10.1021/acs.est.8b04367.
- Kuang, X., Jiao, J.J., Zheng, C., Cherry, J.A., Li, H., 2020. A review of specific storage in aquifers. J. Hydrol. 581, 124282. http://dx.doi.org/10.1016/j.jhydrol.2019.124383.
- Linde, N., Finsterle, S., Hubbard, S., 2006. Inversion of tracer test data using tomographic constraints. Water Resour. Res. 42 (4), http://dx.doi.org/10.1029/ 2004WR003806.
- Madsen, L.M., Fiandaca, G., Auken, E., 2020. 3-D time-domain spectral inversion of resistivity and full-decay induced polarization data full solution of Poisson's equation and modelling of the current waveform. Geophys. J. Int. 223, 2101–2116. http://dx.doi.org/10.1093/gji/ggaa443.
- Madsen, L.M., Fiandaca, G., Auken, E., Christiansen, A.V., 2017. Time-domain induced polarization – an analysis of cole–cole parameter resolution and correlation using Markov chain Monte Carlo inversion. Geophys. J. Int. 211, 1341–1353. http: //dx.doi.org/10.1093/gji/ggx355.

- Marshall, D.J., Madden, T.R., 1959. Induced polarization, a study of its causes. Geophysics 4, 790–816.
- Martin, T., Günther, T., Orozco, A.F., Dahlin, T., 2020. Evaluation of spectral induced polarization field measurements in time and frequency domain. J. Appl. Geophys. 180, 104141. http://dx.doi.org/10.1016/j.jappgeo.2020.104141.
- Martin, T., Pauw, P.S., Karoulis, M., Mendoza, A., Günther, T., Madsen, L.M., Maurya, P.K., Doetsch, J., Rejkjaer, S., Dahlin, T., Fiandaca, G., 2021. Inversion of hydraulic conductivity from induced polarisation, part b: Field examples from five countries. In: NSG2021 1st Conference on Hydrogeophysics. http://dx.doi.org/10.3997/2214-4609.202120093.
- Maurya, P.K., Balbarini, N., Moller, I., Ronde, V., Christiansen, A.V., Bjerg, P.L., Auken, E., Fiandaca, G., 2018a. Subsurface imaging of water electrical conductivity, hydraulic permeability and lithology at contaminated sites by induced polarization. Geophys. J. Int. 213, 770–785. http://dx.doi.org/10.1093/gji/ggy018.
- Maurya, P.K., Fiandaca, G., Christiansen, A.V., Auken, E., 2018b. Field-scale comparison of frequency- and time-domain spectral induced polarization. Geophys. J. Int. 214, 1441–1466. http://dx.doi.org/10.1093/gji/ggy218.
- McLachlan, P., Blanchy, G., Chanbers, J., Sorensen, J., Uhlemann, S., Wilkinson, P., Binley, A., 2021. The application of electromagnetic induction methods to reveal the hydrogeological structure of a riparian wetland. Water Resour. Res. 57 (6), http://dx.doi.org/10.1029/2020WR029221.
- Mollaret, C., Wagner, F., Hilbich, C., Scapozza, C., Hauck, C., 2020. Petrophysical joint inversion applied to alpine permafrost field sites to image subsurface ice, water, air, and rock contents. Front. Earth Sci. 8, 85. http://dx.doi.org/10.3389/feart. 2020.00085
- Olhoeft, G.R., 1985. Low-frequency electrical properties. Geophysics 50 (12), 2492–2503. http://dx.doi.org/10.1190/1.1441880.
- Olsson, P.I., Fiandaca, G., Larsen, J.J., Dahlin, T., Auken, E., 2016. Doubling the spectrum of time-domain induced polarization by harmonic de-noising, drift correction, spike removal, tapered gating and data uncertainty estimation. Geophys. J. Int. 207, 774–784. http://dx.doi.org/10.1093/gji/ggw260.
- Orozco, A.F., Kemna, A., Oberdörster, C., Zschornak, L., Leven, C., Dietrich, P., Weiss, H., 2012. Delineation of subsurface hydrocarbon contamination at a former hydrogenation plant using spectral induced polarization imaging. J. Contam. Hydrol. 136–137, 131–144. http://dx.doi.org/10.1016/j.jconhyd.2012.06.001.
- Pelton, W., Ward, S., Hallof, P., Sill, W., Nelson, P., 1978. Mineral discrimination and removal of inductive coupling with multifrequency IP. Geophysics 43, 588–609. http://dx.doi.org/10.1190/1.1440839.
- Pirot, G., Linde, N., Mariethoz, G., Bradford, J., 2017. Probabilistic inversion with graph cuts: Application to the boise hydrogeophysical research site. Water Resour. Res. 53 (2), 1231–1250. http://dx.doi.org/10.1002/2016WR019347.
- Pouladi, B., Linde, N., Longeuvergne, L., Bour, O., 2021. Individual and joint inversion of head and flux data by geostatistical hydraulic tomography. Adv. Water Resour. 154, 103960. http://dx.doi.org/10.1016/j.advwatres.2021.103960.
- Revil, A., Binley, A., Mejus, L., Kessouri, P., 2015. Predicting permeability from the characteristic relaxation time and intrinsic formation factor of complex conductivity spectra. Water Resour. Res. 51, 6672–6700. http://dx.doi.org/10.1002/ 2015WR017074.
- Revil, A., Florsch, N., 2010. Determination of permeability from spectral induced polarization in granular media. Geophys. J. Int. 181, 1480–1498. http://dx.doi. org/10.1111/j.1365-246X.2010.04573.x.
- Revil, A., Florsch, N., Camerlynck, C., 2014. Spectral induced polarization porosimetry. Geophys. J. Int. 198, 1016–1033. http://dx.doi.org/10.1093/gji/ggu180.
- Revil, A., Karaoulis, M., Johnson, T., Kemna, A., 2012a. Review: Some low-frequency electrical methods for subsurface characterization and monitoring in hydrogeology. Hydrogeol. J. 20, 617–658. http://dx.doi.org/10.1007/s10040-011-0819-x.
- Revil, A., Koch, K., Holliger, K., 2012b. Is it the grain size or the characteristic pore size that controls the induced polarization relaxation time of clean sands and sandstones? Water Resour. Res. 48, http://dx.doi.org/10.1029/2011WR011561.
- Ringel, L.M., Jalali, M., Bayer, P., 2021. Stochastic inversion of three-dimensional discrete fracture network structure with hydraulic tomography. Water Resour. Res. 57 (12), http://dx.doi.org/10.1029/2021WR030401.
- Robinson, J., Slater, L., Weller, A., Keating, K., Robinson, T., Rose, C., Parker, B., 2018. On permeability prediction from complex conductivity measurements using polarization magnitude and relaxation time. Water Resour. Res. 54, 3436–3452. http://dx.doi.org/10.1002/2017WR022034.
- Römhild, L., Sonntag, M., Kiyan, D., Rogers, R., Rath, V., Börner, J.H., 2019. Anisotropic complex electrical conductivity of black shale and mudstone from the moffat shale group (Ireland). Near Surf. Geophys. 17, 675–690. http://dx.doi.org/10.1002/nsg. 12073.
- Rücker, C., Günther, T., Wagner, F.M., 2017. pyGIMLi: An open-source library for modelling and inversion in geophysics. Comput. Geosci. 109, 106–123. http://dx. doi.org/10.1016/j.cageo.2017.07.011.

- Sánchez-León, E., Leven, C., Erdal, D., Cirpka, O.A., 2020. Comparison of two ensemble-kalman filter based methods for estimating aquifer parameters from real 3-d hydraulic and tracer tomographic tests. Geosciences (Switzerland) 10 (11), 1–30. http://dx.doi.org/10.3390/geosciences10110462.
- Schön, J., 2015. Physical Properties of Rocks Fundamentals and Principles of Petrophysics, second ed. In: Handbook of Geophysical Exploration, vol. 18, Elsevier.
- Schwarz, G., 1962. A theory of the low-frequency dielectric dispersion of colloidal particles in electrolyte solution. J. Phys. Chem. 66, 2636–2642.
- Seigel, H.O., 1959. Mathematical formulation and type curves for induced polarization. Geophysics 24, 547–565.
- Slater, L., 2007. Near surface electrical characterization of hydraulic conductivity: From petrophysical properties to aquifer geometries - A review. Surv. Geophys. 28, 169–197. http://dx.doi.org/10.1007/s10712-007-9022-y.
- Slater, L., Lesmes, D.P., 2002. Electrical-hydraulic relationships observed for unconsolidated sediments. Water Resour. Res. 38 (10), 1213. http://dx.doi.org/10.1029/ 2001WP001075
- Tarasov, A., Titov, K., 2013. On the use of the cole-cole equations in spectral induced polarization. Geophys. J. Int. 195, 352–356. http://dx.doi.org/10.1093/gji/ggt251.
- Titov, K., Tarasov, A., Ilyin, Y., Seleznev, N., Boyd, A., 2010. Relationships between induced polarization relaxation time and hydraulic properties of sandstone. Geophys. J. Int. 180, 1095–1106. http://dx.doi.org/10.1111/j.1365-246X.2009.04465.x.
- Turco, F., Azevedo, L., Grana, D., Crutchley, G., Gorman, A., 2021. Characterization of gas hydrate systems on the hikurangi margin (New Zealand) through geostatistical seismic and petrophysical inversion. Geophysics 86 (6), R825–R838. http://dx.doi. org/10.1190/geo2021-0018.1.
- van der Walt, S., Schönberger, J., Nunez-Iglesias, J., Boulogne, F., Warner, J., Yager, N., Gouillart, E., Yu, T., 2014. Scikit-image: Image processing in python. PeerJ 2, e453. http://dx.doi.org/10.7717/peerj.453.
- Vasco, D.W., Keers, H., Karasaki, K., 2000. Estimation of reservoir properties using transient pressure data: An asymptotic approach. Water Resour. Res. 36 (12), http://dx.doi.org/10.1029/2000WR900179.
- Vilhelmsen, T.N., Behroozmand, A.A., Christensen, S., Nielsen, T.H., 2014. Joint inversion of aquifer test, MRS, and TEM data. Water Resour. Res. 50, 3956–3975. http://dx.doi.org/10.1002/2013WR014679.
- Wang, Z., Bovik, A., Sheik, H., Simoncelli, E., 2004. Image quality assessment: From error visibility to structural similarity. IEEE Trans. Image Process. 13 (4), http://dx.doi.org/10.1109/TIP.2003.819861.
- Wang, C., Briggs, M.A., Day-Lewis, F.D., Slater, L.D., 2021. Characterizing physical properties of streambed interface sediments using in situ complex electrical conductivity measurements. Water Resour. Res. 57 (2), http://dx.doi.org/10.1029/ 2020WR027905
- Weller, A., Slater, L., Binley, A., Nordsiek, S., Xu, S., 2015. Permeability prediction based on induced polarization: Insights from measurements on sandstone and unconsolidated samples spanning a wide permeability range. Geophysics 80 (2), D161–D173. http://dx.doi.org/10.1190/GEO2014-0368.1.
- Weller, A., Slater, L., Nordsiek, S., 2013. On the relationship between induced polarization and surface conductivity: Implications for petrophysical interpretation of electrical measurements. Geophysics 78 (5), D315–D325. http://dx.doi.org/10. 1190/GEO2013-0076.1.
- Weller, A., Zhang, Z., Slater, L., Kruschwitz, S., Halisch, M., 2016. Induced polarization and pore radius - A discussion. Geophysics 81 (5), D519–D526. http://dx.doi.org/ 10.1190/GEO2016-0135.1.
- Wu, C.M., Yeh, T.C.J., Zhu, J., Tim, H.L., Hsu, N.S., Chen, C.H., Sancho, A.F., 2005. Traditional analysis of aquifer tests: Comparing apples to oranges? Water Resour. Res. 41 (9), 1–12. http://dx.doi.org/10.1029/2004WR003717.
- Yeh, J., Lee, C.H., 2007. Time to change the way we collect and analyze data for aquifer characterization. Groundwater 45, 116–118. http://dx.doi.org/10.1111/j. 1745-6584.2006.00292.x.
- Yeh, J., Liu, S., 2000. Hydraulic tomography: Development of a new aquifer test method. Water Resour. Res. 36 (8), 2095–2105. http://dx.doi.org/10.1029/
- Yue, W., 2019. Pore-scale explanation of the archie's cementation exponent: Microstructure, electrical anisotropy, and numerical experiments. Geophys. Res. Lett. 46, 5799–5807. http://dx.doi.org/10.1029/2019GL082585.
- Zhao, Z., Illman, W.A., 2018. Three-dimensional imaging of aquifer and aquitard heterogeneity via transient hydraulic tomography at a highly heterogeneous field site. J. Hydrol. 559, 392–410. http://dx.doi.org/10.1016/j.jhydrol.2018.02.024.